AIAA JOURNAL
Vol. 44, No. 4, April 2006

Systematic Analysis of Lean-Premixed Swirl-Stabilized Combustion

Ying Huang,* Shanwu Wang,† and Vigor Yang‡
Pennsylvania State University, University Park, Pennsylvania 16802

A systematic data-analysis procedure is established to explore the underlying mechanisms responsible for driving unsteady flow motions in gas-turbine combustors. Various data processing and analysis approaches are developed and implemented. These include triple decomposition of flowfield, vortex identification, spectral analysis, linear acoustic modal and hydrodynamic stability analyses, and proper orthogonal decomposition. The work allows for a detailed investigation of the mechanisms of energy exchange between the mean, periodic, and turbulent flowfields in a combustion chamber, as well as their collective interactions with chemical heat release. As a specific example, the combustion dynamics in a lean-premixed swirl-stabilized combustor operating under a variety of conditions is carefully examined, based on an avalanche of time-resolved numerical data obtained from large-eddy simulations.

I. Introduction

THE occurrence of combustion instability presents a serious problem in the development of gas-turbine engines, especially for low-emission, lean-premixed systems.[1,2] The instability arises from the coupling between oscillatory flow motions and unsteady combustion and is manifested by self-excited, large-amplitude pressure fluctuations in the combustion chamber. They are highly detrimental to combustor operation and may even cause catastrophic failure in extreme cases. Although several mechanisms responsible for driving combustion instabilities, such as hydrodynamic instabilities,[3] equivalence-ratio fluctuations,[4] and flame surface variations,[5,6] have been proposed and studied, many aspects of physiochemical processes and operating parameters dictating the initiation and sustaining of instabilities are still unresolved. The situation is further complicated for engines that use swirling flow to stabilize the flame with recirculation, which produces a relatively compact flame and modifies the heat release distribution. Swirling flow also tends to induce vortex breakdown and azimuthal instability, thus, it exercises profound influences on the combustion dynamics.[5,7] Fundamental investigations into this issue are strongly needed to further improve our knowledge of combustion instabilities.

The large-eddy simulation (LES) technique is a useful tool for studying gas-turbine combustion dynamics because the flowfields of concern are highly unsteady and dominated by large-scale turbulence motions. Huang et al.[5] reviewed work on the LES of lean-premixed gas-turbine combustion with swirl injectors through 2003. A number of studies have appeared since then. Stone and Menon[8,9] investigated a swirl-stabilized combustor flow using LES modeling. The effects of swirl and equivalence ratio on flame dynamics were studied. Pierce and Moin[10] conducted a numerical simulation of a coaxial jet combustor. A flamelet/progress-variable approach was developed to treat nonpremixed turbulent combustion. Selle et al.[11] treated a full burner of a premixed gas-turbine engine using LES for both nonreacting and reacting cases. A strong precessing vortex core is observed for the nonreacting flows. This vortex, however, disappears when combustion occurs. Grinstein and Fureby[12] simulated the flowfied in a swirl gas combustor, with emphasis on the effects of combustor confinement on the flow and flame evolution. Sommerer et al.[13] conducted an LES study of the flashback and blowoff in a lean partially premixed swirl burner. Wang et al.[14,15] recently examined the vortical flow dynamics in swirl injectors with radial entry under conditions with and without external excitations. Various flow instability mechanisms, such as the Kelvin–Helmholtz, helical, and centrifugal instabilities, as well as their mutual interactions, were investigated in detail. Huang and Yang[16,17] examined the influences of inlet flow conditions on the combustion dynamics in a lean-premixed swirl-stabilized combustor. The flame bifurcation phenomenon and stability boundary were investigated as a function of the burner operating conditions.

The aforementioned LES studies have generated an avalanche of information about the combustion dynamics and flow evolution in specific geometries of concern under well-defined operation conditions. A huge database has been established, which, however, may not lead to a corresponding enhancement of our knowledge if the numerical results are not effectively analyzed. The LES computations themselves represent meticulous exploratory numerical experiments. It is important to be able to extract phenomenological information contributing to understanding and modeling the processes of concern from these large quantities of detailed flow and combustion data. Although various data processing approaches have been employed in the preceding studies, and much useful information has been obtained, a comprehensive and systematic methodology for treating the numerical data is still desired. The present work addresses this important aspect of numerical study by establishing a detailed data analysis procedure, to explore the dynamic processes in gas-turbine combustors and to identify the underlying mechanisms and key parameters dictating the combustion characteristics. As a specific example, the methodology is applied to a time-resolved numerical database for a lean-premixed swirl-stabilized combustor, obtained previously using an LES technique along with a level-set flamelet library approach.[5,17]

The remainder of the paper is organized as follows. In Sec. II the energy transfer mechanisms among the mean, periodic, and turbulent flowfields are examined using a triple decomposition technique. The results provide a theoretical foundation for the analysis of flow oscillations. In Sec. III the relevant information about the LES database, including numerical formulation, boundary condition, physical model, and grid resolution are briefly described. The unsteady flow development and flame dynamics in a lean-premixed swirl-stabilized combustor are studied in Sec. IV by means of various data analysis techniques. These include vortex identification, spectral analysis, linear acoustic modal analysis, linear hydrodynamic stability analysis, and the proper orthogonal decomposition method.

Received 6 January 2005; revision received 1 May 2005; accepted for publication 12 August 2005.

*Postdoctoral Research Associate, Department of Mechanical and Nuclear Engineering. Member AIAA.

†Research Associate, Department of Mechanical and Nuclear Engineering. Member AIAA.

‡Distinguished Professor, Department of Mechanical and Nuclear Engineering; vigor@psu.edu. Fellow AIAA.

II. Energy Transfer Mechanisms in Turbulent Reacting Flows

Both random and periodic (coherent) motions exist in many practical turbulent flows, especially in a gas-turbine combustor. The intricate coupling between these flow motions and flame evolution plays an important role in determining the characteristics of a turbulent reacting flow. It is important to understand the energy transfer mechanisms responsible for driving and sustaining periodic oscillations in a combustor. Reynolds and Hussain[18] and Liu[19] investigated the energy transfer between mean, periodic, and turbulent motions in an incompressible flow using a triple-decomposition technique. The energy of periodic motion is taken as its kinetic energy. The main factor contributing to the growth of periodic motion is the mean correlations between components of the deterministic velocity. The analysis, later, was extended by Wang and Yang[15] and Apte and Yang[20] to accommodate the effect of fluid compressibility using density-weighted Favre averaging.

In compressible flows, the energy of periodic motion includes both kinetic and potential energies. In addition, when combustion takes place, heat release from chemical reactions not only increases the gas temperature and accelerates the bulk flow motions, but also provides an additional energy source for periodic flow motions. The energy transfer mechanisms in a viscous, compressible, heat-conductive medium were investigated by Chu[21] by means of a Reynolds decomposition technique. The effects of body forces, heat, and material sources on the addition of energy to small disturbances were discussed. The transfer of energy from a steady main stream was also examined. Chu,[21] however, did not distinguish periodic motions from background turbulent fluctuations. In the present work, the triple-decomposition technique, which allows the random and periodic motions to be separated from each other, is employed to investigate the energy transfer mechanisms between mean, periodic, and turbulent motions, as well as the influence of heat release on flow dynamics in a turbulent reacting environment. A comprehensive description of the energy exchange mechanisms can be obtained from the following analysis.

A. Triple Decomposition of Flow Variable

Following the approach of Apte and Yang[20] and Huang,[22] each flow variable $\Im$ can be expressed as the sum of density-weighted long-time-averaged $\overleftrightarrow{\Im}$, periodic (coherent) $\Im^a$, and turbulent (stochastic) $\Im^t$ quantities as follows:

$$\Im(\boldsymbol{x}, t) = \overleftrightarrow{\Im}(\boldsymbol{x}) + \Im^a(\boldsymbol{x}, t) + \Im^t(\boldsymbol{x}, t) \tag{1}$$

The decomposition is achieved using the density-weighted long-time- and ensemble-phase averaging techniques, denoted by overbars and carats, respectively, as shown hereafter. For density-weighted long-time averaging

$$\overleftrightarrow{\Im}(\boldsymbol{x}) = \frac{\overline{\rho\Im(\boldsymbol{x})}}{\bar{\rho}}$$

$$\overline{\rho\Im(\boldsymbol{x})} = \left[\lim_{N\to\infty}\frac{1}{N}\sum_{n=0}^{N-1}\rho\Im(\boldsymbol{x}, t_0 + n\Delta t)\right]$$

$$\text{where } N\Delta t \gg \tau \gg \Delta t \tag{2}$$

For density-weighted ensemble-phase averaging

$$\overleftrightarrow{\Im}(\boldsymbol{x}) + \Im^a(\boldsymbol{x}, t) = \frac{\langle\rho\Im(\boldsymbol{x}, t)\rangle}{\langle\rho\rangle}$$

$$\langle\rho\Im(\boldsymbol{x}, t)\rangle = \lim_{N\to\infty}\frac{1}{N}\sum_{n=0}^{N-1}\rho\Im(\boldsymbol{x}, t + n\tau) \tag{3}$$

Thus,

$$\Im^a(\boldsymbol{x}, t) = \langle\rho\Im(\boldsymbol{x}, t)\rangle/\langle\rho\rangle - \overline{\rho\Im(\boldsymbol{x})}/\bar{\rho}$$

$$(\rho\Im)^a = \langle\rho\Im\rangle - \overline{\rho\Im} = \rho^a\overleftrightarrow{\Im} + \bar{\rho}\Im^a + \rho^a\Im^a \tag{4}$$

Here ρ is density, τ is the period of organized oscillation, and t_0 is the temporal location at which steady periodic motions are attained. Some useful properties that follow from the basic definitions of the two averages are

$$\overline{\rho(\Im^a + \Im^t)} = 0, \qquad \langle\rho\Im^t\rangle = 0, \qquad \overline{\Im^a} \neq 0$$

$$\overline{\overleftrightarrow{\Im}\Re} = \overleftrightarrow{\Im}\overline{\Re}, \qquad \langle\Im^a\Re\rangle = \Im^a\langle\Re\rangle, \qquad \langle\overleftrightarrow{\Im}\Re\rangle = \overleftrightarrow{\Im}\langle\Re\rangle$$

$$\overline{\langle\Im\rangle} = \overline{\Im}, \qquad \langle\Im^a\rangle = \Im^a, \qquad \overline{\rho\Im^a\Re^t} = \overline{\langle\rho\Im^a\Re^t\rangle} = 0 \tag{5}$$

The last relation states that the density-weighted periodic and turbulent motions are uncorrelated on average. Evaluation of the ensemble-phase average in Eq. (3) requires calculation and storage of an avalanche of data to achieve statistically consistent and meaningful results. To bypass this computational difficulty, a windowed Fourier transform is normally used to extract the deterministic motion from the original time-trace data by choosing the Fourier component at the frequency of concern.[20]

The averaged kinetic energy per unit volume is defined as follows:

$$\kappa = \overline{\rho u_i u_i}/2 = \bar{\rho}\overleftrightarrow{u}_i\overleftrightarrow{u}_i/2 + \bar{\rho}\,\overleftrightarrow{u_i^a u_i^a}\big/2 + \bar{\rho}\,\overleftrightarrow{u_i^t u_i^t}\big/2 \tag{6}$$

The energy associated with periodic motion ε contains both kinetic ε_k and potential ε_p energies, in accordance to acoustic theories,

$$\varepsilon = \varepsilon_k + \varepsilon_p = \bar{\rho}\,\overleftrightarrow{u_i^a u_i^a}\big/2 + \overline{(p^a)^2}/(2\bar{\rho}\cdot\bar{c}^2) \tag{7}$$

B. Mean, Deterministic, and Turbulent Motion

The mass, momentum, and energy balances for an ideal gas mixture can be written in the following conservation form:

$$\frac{\partial\rho}{\partial t} + \frac{\partial(\rho u_j)}{\partial x_j} = 0 \tag{8}$$

$$\frac{\partial(\rho u_i)}{\partial t} + \frac{\partial(\rho u_i u_j)}{\partial x_j} = -\frac{\partial p}{\partial x_i} + \frac{\partial\sigma_{ij}}{\partial x_j} \tag{9}$$

$$\frac{\partial(\rho c_v T)}{\partial t} + \frac{\partial(\rho u_j c_v T)}{\partial x_j} = -\frac{\partial\dot{q}_i''}{\partial x_i} - p\frac{\partial u_j}{\partial x_j} + \Phi + \dot{q} \tag{10}$$

where u_i, p, and T represent the velocity component in the ith spatial direction, pressure, and temperature. Here, σ_{ij}, $\dot{q}_i''$, and Φ are the viscous stress tensor, heat flux due to conduction and species diffusion, and viscous dissipation, respectively; $\dot{q}$ is the rate of heat release from chemical reactions. Equation (10) can be rearranged using the equation of state with the assumption of constant specific heat ratio γ to become

$$\frac{\partial p}{\partial t} + u_j\frac{\partial p}{\partial x_j} = -\gamma p\frac{\partial u_j}{\partial x_j} + (\gamma - 1)\left(-\frac{\partial\dot{q}_i''}{\partial x_i} + \Phi + \dot{q}\right) \tag{11}$$

When the decomposed flow variables defined in Eqs. (2–4) are applied to Eq. (8), the continuity equations for the mean, deterministic, and turbulent flowfields are obtained,

$$\frac{\partial\bar{\rho}}{\partial t} + \frac{\partial(\bar{\rho}\overleftrightarrow{u}_j)}{\partial x_j} = 0 \tag{12}$$

$$\frac{\partial\rho^a}{\partial t} + \frac{\partial(\langle\rho\rangle u_j^a + \rho^a\overleftrightarrow{u}_j)}{\partial x_j} = 0 \tag{13}$$

$$\frac{\partial\rho^t}{\partial t} + \frac{\partial(\langle\rho\rangle u_j^t + \rho^t u_j)}{\partial x_j} = 0 \tag{14}$$

Note that only the velocity components and temperature are needed to average with density to avoid density–velocity correlations in the momentum equations and density–temperature correlations in the energy equation. Other flow variables, such as density, pressure, and stresses, are decomposed into long-time-averaged, periodic, and stochastic quantities in the following derivations.

The momentum equation for the mean flowfield is obtained by taking the long-time average of Eq. (9),

$$\frac{\partial(\bar{\rho}\overleftrightarrow{u}_i\overleftrightarrow{u}_j)}{\partial x_j} = -\frac{\partial\left(\overline{\rho u_i^a u_j^a}\right)}{\partial x_j} - \frac{\partial\left(\overline{\rho u_i^t u_j^t}\right)}{\partial x_j} - \frac{\partial \bar{p}}{\partial x_i} + \frac{\partial \bar{\sigma}_{ij}}{\partial x_j} \tag{15}$$

The momentum equation for periodic motion is derived by taking the ensemble-phase average of Eq. (9) and subtracting Eq. (15),

$$\langle\rho\rangle\frac{\partial u_i^a}{\partial t} + \langle\rho\rangle(\overleftrightarrow{u}_j + u_j^a)\frac{\partial u_i^a}{\partial x_j} = -\langle\rho\rangle u_j^a\frac{\partial \overleftrightarrow{u}_i}{\partial x_j}$$
$$-\frac{\partial\left(\rho u_i^t u_j^t\right)^a}{\partial x_j} + \frac{\partial\left(\overline{\rho u_i^a u_j^a}\right)}{\partial x_j} - \frac{\partial p^a}{\partial x_i} + \frac{\partial \sigma_{ij}^a}{\partial x_j} - \frac{\rho^a \aleph_{\overleftrightarrow{u},i}}{\bar{\rho}} \tag{16}$$

The momentum equation for turbulent fluctuations is obtained by taking the ensemble phase average of Eq. (9) and subtracting the resultant equation from Eq. (9),

$$\rho\frac{\partial u_i^t}{\partial t} + \rho\left(\overleftrightarrow{u}_j + u_j^a\right)\frac{\partial u_i^t}{\partial x_j} = -\rho u_j^t\frac{\partial \overleftrightarrow{u}_i}{\partial x_j} - \rho u_j^t\frac{\partial u_i^a}{\partial x_j} + u_i^t\frac{\partial \rho u_j^t}{\partial x_j}$$
$$-\frac{\partial\left(\rho u_i^t u_j^t\right)^t}{\partial x_j} - \frac{\partial p^t}{\partial x_i} + \frac{\partial \sigma_{ij}^t}{\partial x_j} - \frac{\rho^t \aleph_{\langle u\rangle,i}}{\langle\rho\rangle} \tag{17}$$

In Eqs. (16) and (17), $\aleph_{\overleftrightarrow{u},i}$ and $\aleph_{\langle u\rangle,i}$ represent the net forces on a fluid element in the long-time-averaged and phase-averaged flowfields, which can be written as

$$\aleph_{\overleftrightarrow{u},i} = -\frac{\partial\left(\overline{\rho u_i^a u_j^a}\right)}{\partial x_j} - \frac{\partial\left(\overline{\rho u_i^t u_j^t}\right)}{\partial x_j} - \frac{\partial \bar{p}}{\partial x_i} + \frac{\partial \bar{\sigma}_{ij}}{\partial x_j} \tag{18}$$

$$\aleph_{\langle u\rangle,i} = -\frac{\partial\left\langle\rho u_i^t u_j^t\right\rangle}{\partial x_j} - \frac{\partial\langle p\rangle}{\partial x_i} + \frac{\partial\langle\sigma_{ij}\rangle}{\partial x_j} \tag{19}$$

The last terms $\rho^a\aleph_{\overleftrightarrow{u},i}/\bar{\rho}$ and $\rho^t\aleph_{\langle u\rangle,i}/\langle\rho\rangle$ in Eqs. (16) and (17) can be neglected, providing that $\rho^a \ll \bar{\rho}$ and $\rho^t \ll \bar{\rho}$.

Each of the preceding momentum equations contains a part of the nonlinear term $-\rho u_i^t u_j^t$. The time-averaged component $-\overline{\rho u_i^t u_j^t}$, which is the Reynolds stress of turbulent flow, appears in the time-averaged momentum equation (15). The periodic component $-(\rho u_i^t u_j^t)^a$ is found in the momentum equation for organized oscillations (16). The remaining component $-(\rho u_i^t u_j^t)^t$ is present in the momentum equation for stochastic motions (17). The term $-\overline{\rho u_i^a u_j^a}$, which represents the mean correlation between the deterministic velocity components, appears in both Eqs. (15) and (16). These terms play important roles in the mechanism of energy transfer between mean, periodic, and turbulent motions, as will be shown later.

C. Kinetic Energy Transfer Between Mean, Organized, and Turbulent Flowfields

The equation for the kinetic energy $\bar{\rho}\overleftrightarrow{u}_i\overleftrightarrow{u}_i/2$ is derived by multiplying Eq. (15) by $\overleftrightarrow{u}_i$. Rearranging the result and using the continuity equation, we have

$$\frac{\partial(\overleftrightarrow{u}_j\bar{\rho}\overleftrightarrow{u}_i\overleftrightarrow{u}_i/2)}{\partial x_j} = \overline{\rho u_i^a u_j^a}\frac{\partial \overleftrightarrow{u}_i}{\partial x_j} + \overline{\rho u_i^t u_j^t}\frac{\partial \overleftrightarrow{u}_i}{\partial x_j} - \frac{\partial\left(\overleftrightarrow{u}_i\overline{\rho u_i^a u_j^a} + \overleftrightarrow{u}_i\overline{\rho u_i^t u_j^t}\right)}{\partial x_j}$$
$$+\bar{p}\frac{\partial \overleftrightarrow{u}_i}{\partial x_i} + \frac{\partial[\overleftrightarrow{u}_i(\bar{\sigma}_{ij} - \bar{p})]}{\partial x_j} - \bar{\sigma}_{ij}\frac{\partial \overleftrightarrow{u}_i}{\partial x_j} \tag{20}$$

The equation for $\bar{\rho}\overline{u_i^a u_j^a}/2$ is formed by multiplying Eq. (16) by u_i^a, taking a time average, and rearranging the result,

$$\frac{\partial\left(\bar{\rho}\overleftrightarrow{u_i^a u_i^a}/2\right)}{\partial t} + \frac{\partial\left(\bar{\rho}\overleftrightarrow{u}_j\overleftrightarrow{u_i^a u_i^a}/2\right)}{\partial x_j} + \frac{\partial\overline{\left(\rho u_j^a u_i^a u_i^a/2\right)}}{\partial x_j}$$
$$= -\overline{\rho u_i^a u_j^a}\frac{\partial \overleftrightarrow{u}_i}{\partial x_j} + \overline{\left(\rho u_i^t u_j^t\right)^a\frac{\partial u_i^a}{\partial x_j}} - \frac{\partial\overline{u_i^a p^a}}{\partial x_i} + \overline{p^a\frac{\partial u_i^a}{\partial x_i}}$$
$$-\overline{\rho u_i^a u_j^a}\frac{\partial\overline{u_i^a}}{\partial x_j} - \frac{\partial\overline{\left\{u_i^a\left[\left(\rho u_i^t u_j^t\right)^a - \overline{\rho u_i^a u_j^a}\right]\right\}}}{\partial x_j}$$
$$+\frac{\partial\overline{u_i^a\sigma_{ij}^a}}{\partial x_j} - \overline{\sigma_{ij}^a\frac{\partial u_i^a}{\partial x_j}} - \frac{\overline{u_i^a\rho^a\aleph_{\overleftrightarrow{u},i}}}{\bar{\rho}} \tag{21}$$

The equation for $\bar{\rho}\overleftrightarrow{u_i^t u_i^t}/2$ can be similarly obtained by multiplying Eq. (17) by u_i^t, taking a time average, and rearranging the result,

$$\frac{\partial}{\partial t}\left(\frac{\bar{\rho}\overleftrightarrow{u_i^t u_i^t}}{2}\right) + \frac{\partial}{\partial x_j}\left(\frac{\bar{\rho}\overleftrightarrow{u}_j\overleftrightarrow{u_i^t u_i^t}}{2}\right) + \frac{\partial}{\partial x_j}\left(\frac{\overline{\rho u_j^a u_i^t u_i^t}}{2}\right)$$
$$= -\overline{\rho u_i^t u_j^t}\frac{\partial \overleftrightarrow{u}_i}{\partial x_j} - \overline{\left(\rho u_i^t u_j^t\right)^a\frac{\partial u_i^a}{\partial x_j}} - \overline{\rho u_i^t u_j^t}\frac{\partial\overline{u_i^a}}{\partial x_j}$$
$$-\overline{\left(\rho u_i^t u_j^t\right)^t\frac{\partial u_i^a}{\partial x_j}} - \frac{\partial\left(\overline{\rho u_j^t u_i^t u_i^t/2}\right)}{\partial x_j} + \frac{\partial\left(\overline{u_i^t\left\langle\rho u_i^t u_j^t\right\rangle}\right)}{\partial x_j}$$
$$-\overline{\left\langle\rho u_i^t u_j^t\right\rangle\frac{\partial u_i^t}{\partial x_j}} - \overline{\left\langle\rho u_i^t u_j^t\right\rangle\frac{\partial u_i^t}{\partial x_j}} - \overline{u_i^t\frac{\partial p^t}{\partial x_i}}$$
$$+\frac{\partial\overline{u_i^t\sigma_{ij}^t}}{\partial x_j} - \overline{\sigma_{ij}^t\frac{\partial u_i^t}{\partial x_j}} - \frac{\overline{u_i^t\rho^t\aleph_{\langle u\rangle,i}}}{\langle\rho\rangle} \tag{22}$$

Each kinetic energy equation contains convection, production, pressure work, and dissipation terms. The production terms are of particular interest in understanding the energy exchange among the three constituent flowfields. The term $\overline{\rho u_i^t u_j^t}\partial\overleftrightarrow{u}_i/\partial x_j$ serves as a pathway for exchanging the kinetic energy between the mean and turbulent fields. The term $\overline{\rho u_i^a u_j^a}\partial\overleftrightarrow{u}_i/\partial x_j$ characterizes the energy transfer between the mean and deterministic fields and provides a basis for explaining the phenomena of flow-turning loss and acoustic streaming. The former refers to the loss of acoustic energy to the mean flow due to misalignment between the acoustic and mean flow velocities.[20] The latter describes the modification of the mean flowfield due to impressed periodic excitation. The energy exchange between the deterministic and turbulent fields is characterized by the term $\overline{(\rho u_i^t u_j^t)^a\partial u_i^a/\partial x_j}$. Obviously, the introduction of organized flow oscillations provides an additional pathway to transfer energy from the mean flowfield to turbulent motion in comparison with stationary flow conditions. The viscous dissipation terms in these three energy equations, that is, $\bar{\sigma}_{ij}\partial\overleftrightarrow{u}_i/\partial x_j$, $\overline{\sigma_{ij}^a\partial u_i^a/\partial x_j}$, and $\overline{\sigma_{ij}^t\partial u_i^t/\partial x_j}$, can also be found in the time-averaged thermal energy equation, as will be shown later, accounting for the transfer between kinetic and internal energy.

D. Potential Energy and Heat Release

The equation for the potential energy of periodic motions, $\varepsilon_p = \overline{(p^a)^2}/(2\bar{\rho}\cdot\bar{c}^2)$, can be obtained by manipulating Eq. (11):

$$\frac{\partial[\overline{(p^a)^2}/(2\bar{\rho}\cdot\bar{c}^2)]}{\partial t} + \overleftrightarrow{u}_j\frac{\partial[\overline{(p^a)^2}/(2\bar{\rho}\cdot\bar{c}^2)]}{\partial x_j} + \overline{u_j^a\frac{\partial[(p^a)^2/(2\bar{\rho}\cdot\bar{c}^2)]}{\partial x_j}}$$
$$= -\overline{p^a\frac{\partial u_j^a}{\partial x_j}} - \frac{\overline{p^a u_j^a}}{\gamma\bar{p}}\frac{\partial\bar{p}}{\partial x_j} - \overline{\frac{(p^a)^2}{\bar{p}}\frac{\partial\left(\overleftrightarrow{u}_j + u_j^a\right)}{\partial x_j}}$$
$$+\frac{(\gamma-1)}{\gamma\bar{p}}\cdot\left\{\overline{p^a\left(\rho RT^t\frac{\partial u_j^t}{\partial x_j}\right)^a} + \overline{\cdot p^a\left[-\left(\frac{\partial\dot{q}_i''}{\partial x_i}\right)^a + \Phi^a\right]}\right.$$
$$\left.+\overline{p^a\dot{q}^a}\right\} - \overline{\frac{p^a}{\gamma\bar{p}}\cdot\frac{\partial\left[R\left(\rho u_j^t T^t\right)^a\right]}{\partial x_j}} - \overline{\left(\frac{p^a}{\bar{p}}\right)^2\frac{\aleph_{\bar{p}}}{2\gamma}} \tag{23}$$

where $\aleph_{\bar{p}} = \partial\bar{p}/\partial t + (\overleftrightarrow{u}_j + u_j^a)\partial\bar{p}/\partial x_j$.

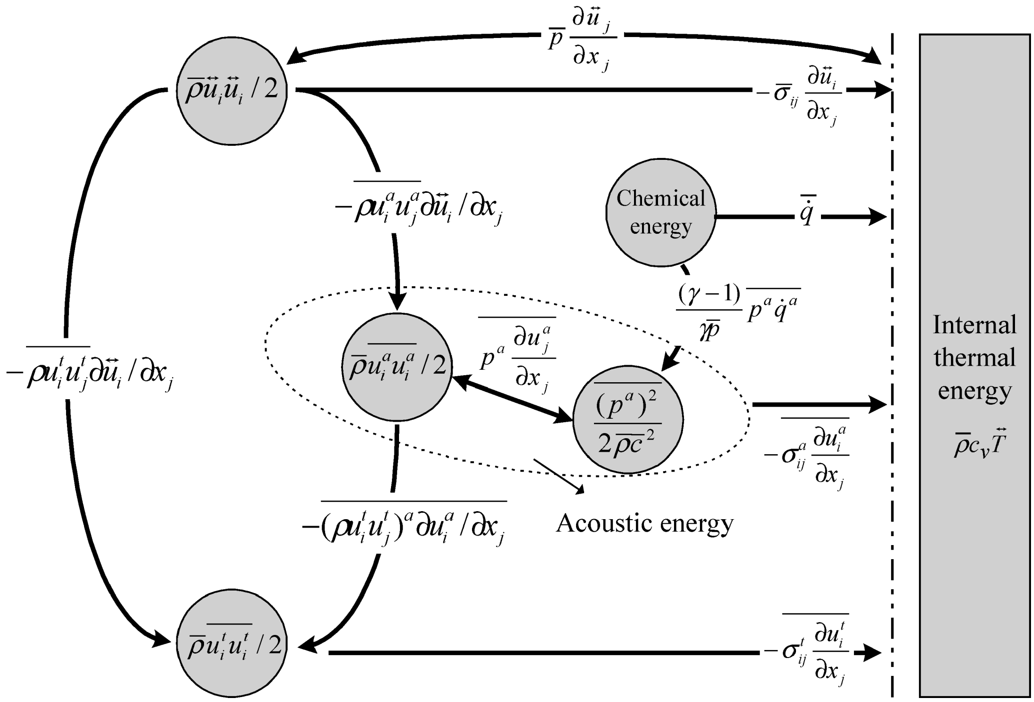

Fig. 1 Mechanisms of energy exchange among mean, periodic, and stochastic motion in turbulent reacting flows.

Combining Eqs. (21) and (23), we obtain the equation for total energy of periodic motions ε based on the definition given in Eq. (7),

$$
\begin{aligned}
&\frac{\partial\bar{\varepsilon}}{\partial t}+\overleftrightarrow{u}_j\frac{\partial\bar{\varepsilon}}{\partial x_j}+\overline{u_j^a\frac{\partial\varepsilon}{\partial x_j}}+\frac{\partial\overline{u_j^a p^a}}{\partial x_j}\\
&\quad=\frac{\overline{p^a u_j^a}}{\gamma\bar{p}}\cdot\frac{\partial\bar{p}}{\partial x_j}-\overline{\frac{(p^a)^2}{\bar{p}}\cdot\frac{\partial\left(\overleftrightarrow{u}_j+u_j^a\right)}{\partial x_j}}-\overline{\rho u_i^a u_j^a}\frac{\partial\overleftrightarrow{u}_i}{\partial x_j}\\
&\qquad+\overline{\left(\rho u_i^t u_j^t\right)^a\frac{\partial u_i^a}{\partial x_j}}+\frac{(\gamma-1)}{\gamma\bar{p}}\cdot\overline{p^a\left(-\left(\frac{\partial\dot{q}_i''}{\partial x_i}\right)^a+\Phi^a\right)}\\
&\qquad+\frac{(\gamma-1)}{\gamma\bar{p}}\cdot\overline{p^a\dot{q}^a}+\frac{\partial\overline{u_i^a\sigma_{ij}^a}}{\partial x_j}-\overline{\sigma_{ij}^a\frac{\partial u_i^a}{\partial x_j}}\\
&\qquad-\overline{\frac{p^a}{\gamma\bar{p}}\cdot\frac{\partial\left[R\left(\rho u_j^t T^t\right)^a\right]}{\partial x_j}}+\frac{(\gamma-1)}{\gamma\bar{p}}\cdot\overline{p^a\left(\rho R T^t\frac{\partial u_j^t}{\partial x_j}\right)^a}\\
&\qquad-\left(\frac{\bar{\rho}u_i^a u_i^a}{2}\right)\cdot\frac{\partial\overleftrightarrow{u}_j}{\partial x_j}-\overline{\left(\rho u_i^a u_i^a/2\right)\frac{\partial u_j^a}{\partial x_j}}-\overline{\rho u_i^a u_j^a}\frac{\partial\overline{u_i^a}}{\partial x_j}\\
&\qquad-\frac{\partial\left\{\overline{u_i^a\left[\left(\rho u_i^t u_j^t\right)^a-\overline{\rho u_i^a u_j^a}\right]}\right\}}{\partial x_j}-\overline{\left(\frac{p^a}{\bar{p}}\right)^2\frac{\aleph_{\bar{p}}}{2\gamma}}-\frac{\overline{u_i^a\rho^a\aleph_{\overleftrightarrow{u},i}}}{\bar{\rho}}
\end{aligned}
\tag{24}
$$

Finally, the transport of mean thermal energy can be obtained from the long-time average of Eq. (10),

$$
\begin{aligned}
&\frac{\partial(\bar{\rho}c_v\overleftrightarrow{T})}{\partial t}+\frac{\partial(\bar{\rho}\overleftrightarrow{u}_j c_v\overleftrightarrow{T})}{\partial x_j}=-\frac{\partial\left(\overline{\rho u_j^a c_v T^a}\right)}{\partial x_j}-\frac{\partial\left(\overline{\rho u_j^t c_v T^t}\right)}{\partial x_j}\\
&\qquad-\frac{\partial\overline{\dot{q}_i''}}{\partial x_i}-\overline{p\frac{\partial u_j}{\partial x_j}}+\bar{\sigma}_{ij}\frac{\partial\overleftrightarrow{u}_i}{\partial x_j}+\overline{\sigma_{ij}^a\frac{\partial u_i^a}{\partial x_j}}+\overline{\sigma_{ij}^t\frac{\partial u_i^t}{\partial x_j}}\\
&\qquad+\bar{\sigma}_{ij}\overline{\frac{\partial\left(u_i^a+u_i^t\right)}{\partial x_j}}+\overline{\sigma_{ij}^a\frac{\partial\left(\overleftrightarrow{u}_i+u_i^t\right)}{\partial x_j}}+\overline{\sigma_{ij}^t\frac{\partial\left(\overleftrightarrow{u}_i+u_i^a\right)}{\partial x_j}}+\bar{\dot{q}}
\end{aligned}
\tag{25}
$$

The term $\overline{p^a\partial u_j^a/\partial x_j}$ appears in both Eqs. (21) and (23), but with opposite signs. It facilitates the exchange between the kinetic ε_k and the potential ε_p energies. When p^a and $\partial u_j^a/\partial x_j$ are in phase, energy flows from its potential to its kinetic component and vice versa. The convection of the energy flux $\partial\overline{u_j^a p^a}/\partial x_j$ on the left-hand side of Eq. (24) represents the transport of acoustic energy within the flowfield. This term vanishes on integration over the entire flowfield for a closed system without energy flow across the boundary.

The source term $(\gamma-1)\overline{p^a\dot{q}^a}/\gamma\bar{p}$ on the right-hand side of Eq. (24) represents the contribution from unsteady heat release. Let θ be the phase difference between pressure and heat release oscillations, then

$$
\frac{(\gamma-1)\overline{p^a\dot{q}^a}}{\gamma\bar{p}}=\frac{(\gamma-1)|p^a\dot{q}^a|\cos\theta}{\gamma\bar{p}}\tag{26}
$$

If the oscillations of pressure and heat release are in phase ($-\pi/2<\theta<\pi/2$), this term is positive, and energy is supplied to the oscillatory flowfield. Otherwise, energy is subtracted from the system for $\pi/2<\theta<3\pi/4$. This result is closely related to the well-known Rayleigh criterion. The unsteady heat flux $-(\partial\dot{q}_i''/\partial x_i)^a$ and dissipation Φ^a terms play a similar role in driving flow oscillations as unsteady heat release, as shown in Eq. (24), but their effects are not as significant as the heat release term. The effect of viscous dissipation, $\Phi=\sigma_{ij}\partial u_i/\partial x_j$, is twofold. It always converts the oscillatory flow energy into its thermal counterpart, but it also tends to increase the energy of periodic motion, when in phase with pressure fluctuation.

The energy exchange mechanisms in a turbulent reacting flow are shown in the schematic diagram in Fig. 1. The oscillatory motions can acquire energy through several different pathways. They may extract energy from the mean flowfield and chemical reactions, exchange energy with background turbulent motion, or be dissipated into thermal energy through viscous damping. When there are no chemical reactions, the primary energy provider for periodic motions is the mean flowfield and/or boundary effects. With combustion, heat release from chemical reactions is the major power source for driving periodic motions. The transfer of energy from chemical reactions to the periodic flowfield only takes place when heat release is in phase with pressure oscillation. These results provide a theoretical foundation for the analysis of oscillatory flowfields in gas-turbine combustors.

III. LES Database

The LES database was established by simulating the flowfields of a lean-premixed swirl-stabilized combustor, operating under a variety of conditions.[5,16,17] The formulation employs the Favre-filtered conservation equations of mass, momentum, and energy in three dimensions. The subgrid-scale (SGS) terms are modeled using a compressible-flow version of the Smagorinsky model suggested by Erlebacher et al.[23] The damping function of Van Driest is used to take into account the flow inhomogeneities near the walls. A level-set flamelet library approach[5] is applied to simulate premixed turbulent combustion. In this approach, the evolution of the filtered flame surface is modeled using a level-set G-equation, where G is defined as a distance function outside the flame front. Thermophysical properties are obtained using a presumed probability density function along with a laminar flamelet library. Although the model does not explicitly consider the flame stretch effect, which may alter the local flame structure and cause flame extinction or liftoff, it has been shown to be able to capture the salient features of unsteady turbulent flame behavior.[5]

Boundary conditions must be specified to complete the formulation. At the inlet boundary, the mass flow rate and temperature are specified. The pressure is obtained from a one-dimensional approximation to the axial momentum equation, that is, $\partial p/\partial x = -\rho \partial u/\partial t - \rho u \partial u/\partial x$. The mean axial-velocity distribution follows the one-seventh power law by assuming a fully developed turbulent pipe flow. The radial and azimuthal velocities are determined from the swirler vane angle. Turbulence properties at the inlet are specified by superimposing broadband disturbances with an intensity of 15% of the mean quantity onto the mean velocity profiles. In addition, the acoustic response to disturbances arising from downstream is modeled by means of an impedance function.[5] At the outlet boundary, the characteristic conditions proposed by Poinsot and Lele[24] are applied, and a time-invariant backpressure is specified. Finally, the no-slip adiabatic conditions are enforced along all of the solid walls.

The resultant governing equations and boundary conditions are solved numerically by means of a density-based, finite volume methodology. The spatial discretization employs a second-order, central-differencing method in generalized coordinates. Fourth-order matrix dissipation, along with a total-variation-diminishing switch developed by Swanson and Turkel[25] and tested by Oefelein and Yang,[26] are included to ensure computational stability and to prevent numerical oscillations in regions with steep gradients. Temporal discretization is obtained using a four-step Runge–Kutta integration scheme. A multiblock domain decomposition technique, along with static load balance, is used to facilitate the implementation of parallel computation with a message passing interface at the domain boundaries. Error analysis of the numerical scheme has been performed using the methods developed by Apte and Yang[27] and Lu et al.[28] The effects of Courant–Friedrichs–Lewy number, artificial dissipation, and SGS terms on the calculated turbulent energy spectrum are carefully examined. The results indicate that the present numerical method offers a reasonable predictive capability for turbulent flows because of its relatively low dissipation and high accuracy. The theoretical and numerical framework described earlier has been validated by Apte and Yang,[29] Huang et al.,[5] Huang,[22] and Lu et al.[28] against a wide variety of flow problems to establish its credibility and accuracy.

The physical model considered herein consists of a single swirl injector, an axi-symmetric chamber, and a choked nozzle, simulating the experiment conducted by Broda et al.[30] and Seo.[31] Gaseous methane is injected radially from the centerbody through 10 holes immediately downstream of the swirler vanes. The fuel/air mixture is assumed to be perfectly premixed before entering the combustor. The chamber measures 45 mm in diameter and 235 mm in length. The baseline condition includes an equivalence ratio of 0.573 and a chamber pressure of 0.463 MPa. The mass flow rates of the natural gas and air are 1.71 and 50.70 g/s, respectively. The inlet flow velocity of 86.6 m/s gives rise to a Reynolds number of 3.5×10^4 based on the height of the inlet annulus. The inlet temperature of 660 K corresponds to the case of unstable combustion reported in Refs. 30 and 31. Two different swirl angles of 30 and 55 deg are investigated in the current study. The corresponding swirl numbers, defined as the ratio of the axial flux of the tangential momentum to the product of the axial momentum flux and a characteristic radius, are 0.44 and 1.10, respectively.

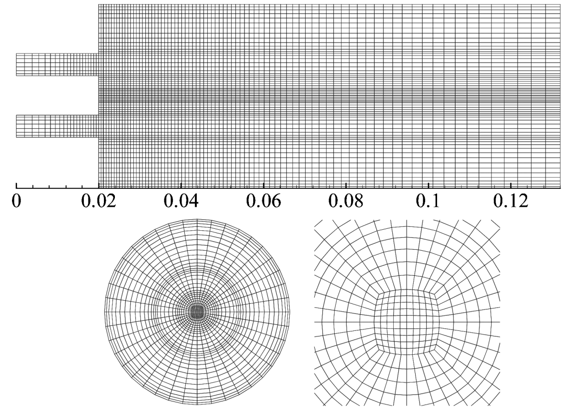

Fig. 2 Schematic of grid system, 3.44 million total grid points, every second, third, and fifth grid point in azimuthal, axial, and radial directions, respectively, are shown.

According to the experimental observations, the dominant acoustic motion in the axial direction corresponds to the first longitudinal mode. Because there exists an acoustic pressure node at the middle of the chamber, the computational domain includes a portion of the inlet annulus downstream of the swirler vane and the upstream half of the chamber with a time-invariant backpressure specified at the exit plane. To avoid the numerical singularity along the combustor centerline, a central-square grid system, which consists of a square grid near the centerline and a cylindrical grid in the outer region, is adopted as shown in Fig. 2. The entire grid system has approximately 3.44 million ($301 \times 141 \times 81$) points, which are clustered in the shear layers downstream of the dump plane and near the solid walls to resolve the steep flow gradients in these regions. The largest grid spacing (around 0.7 mm) falls in the inertial subrange of the turbulent kinetic energy spectrum based on the inlet Reynolds number. The computational domain is divided into 72 blocks. All of the calculations are conducted on a distributed-memory parallel computer with each block calculated on a single processor.

For each swirl number, calculations were performed for about four flow-through times (around 12 ms) after the flowfield had reached its stationary state to obtain statistically meaningful data for analyzing the flow dynamics.

IV. Data Analysis

The section presents detailed descriptions of flow and flame structures. Various data-analysis approaches, including vortex identification, spectral analysis, and linear acoustic-modal and hydrodynamic-stability analyses, are employed to provide direct insights into the combustion dynamics. The proper orthogonal decomposition (POD) technique is then introduced. It is used along with the triple-decomposition technique to investigate the energy exchange mechanisms in the flowfields.

A. Instantaneous Flow and Flame Structures

Figures 3 and 4 show snapshots of the vorticity-magnitude and temperature fields on the x–r and r–θ planes for two different swirl numbers. In both cases, the temperature fields clearly exhibit enveloped flames anchored at the rim of the centerbody and the corner of the backward-facing step. The flame is much more compact for the high-swirl-number case with $S = 1.10$, mainly due to the enhanced flame speed resulting from the increased turbulence intensity.[17] For the low-swirl-number case with $S = 0.44$, large vortical structures arise in the shear layers downstream of the dump plane. In addition to the swirl-induced vorticity, the volume dilation and baroclinic effects in the flame zone significantly contribute to the production of vorticity. These vorticies are convected downstream, break up into small-scale eddies, and are eventually dissipated by turbulent diffusion and viscous damping. The same phenomenon is also observed for the high-swirl-number case, in which well-organized vortices are

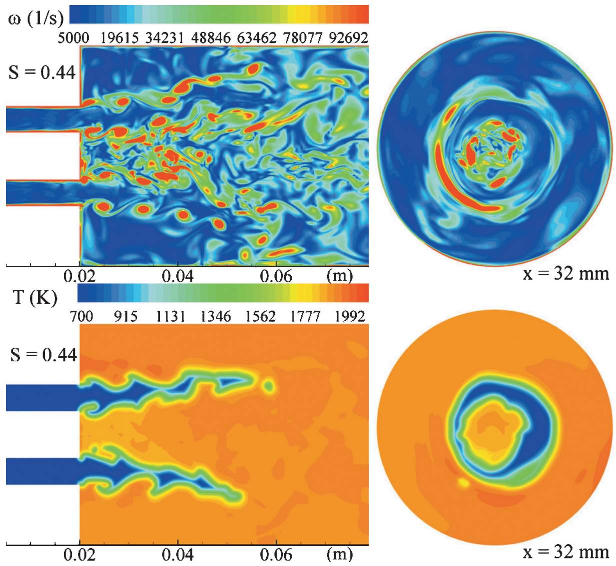

Fig. 3 Snapshots of vorticity-magnitude and temperature field on *x–r* and *r–θ* planes for $S = 0.44$.

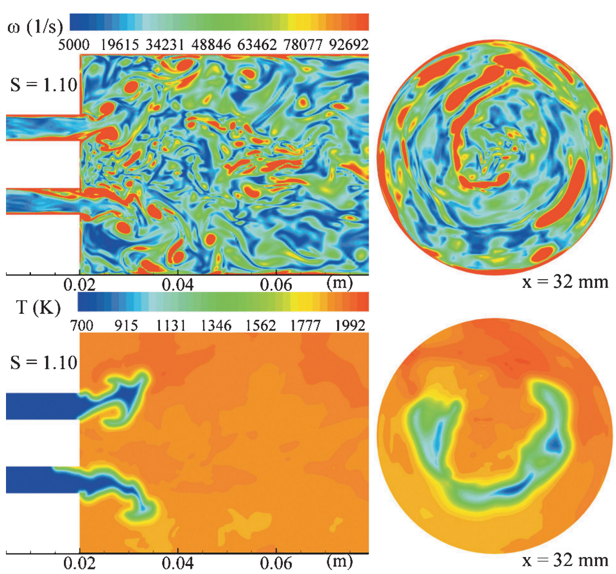

Fig. 4 Snapshots of vorticity-magnitude and temperature field on *x–r* and *r–θ* planes for $S = 1.10$.

shed from the edge of the backward-facing step. The vortex motions downstream of the centerbody, however, become quite disordered due to the existence of a strong central recirculating flow. For both swirl numbers, the vortex shedding frequencies are close to that of the first tangential mode of acoustic wave in the chamber. Flames are contorted and convoluted by these vortex structures, thus revealing the interactions between the local flow evolution and the flame dynamics.

B. Vortex Identification

Vorticity is commonly used to detect coherent structures in free shear flows because these structures manifest themselves as vortices. For wall-bounded flows, however, the use of vorticity to characterize flow evolution has a drawback. The vortical field inherent in the near-wall region may override the vortices originating in the freestream, thereby rendering the examination of flow evolution a challenging task. To overcome this difficulty, several vortex identification techniques have been proposed, including the Δ criterion,[32] Q-criterion[33] and λ_2 criterion.[34] Jeong and Hussain[34] compared these detection algorithms and found that the λ_2 criterion is able to represent the topology and geometry of vortex cores correctly for most of the flows considered in their study. These flows include an inviscid streamwise vortex in a homogeneous shear flow, an elliptic vortex ring, a conically symmetric vortex, a mixing layer, a circular jet, and a Bodewadt vortex. The λ_2 criterion is based on the expectation that the rotational motion associated with a vortex creates a local pressure minimum in its core to ensure the balance between the pressure gradient and the centrifugal force. In practice, however, unsteady straining and viscous effects may lead to discrepancies between the locations of the vortex core and the local pressure minimum. Because the information about local pressure extrema is contained in the Hessian of pressure, $\partial^2 p/\partial x_i \partial x_j$, Jeong and Hussain[34] proposed utilizing the equation for $\partial^2 p/\partial x_i \partial x_j$, which can be derived from the momentum equation for an incompressible flow as follows, to help explore the vortical flow structure:

$$\frac{\mathrm{d}S_{ij}}{\mathrm{d}t} - v\frac{\partial^2 S_{ij}}{\partial x_k \partial x_k} + \Omega_{ik}\Omega_{kj} + S_{ik}S_{kj} = -\frac{1}{\rho}\frac{\partial^2 p}{\partial x_i \partial x_j} \tag{27}$$

where Ω and S are the asymmetric and symmetric components of $\nabla \boldsymbol{u}$. The first two terms in the preceding equation represent unsteady straining and viscous effects, respectively. If we neglect these two terms, a variational analysis indicates that the pressure attains a local minimum if and only if λ_2 is negative, where λ_2 is one of the three eigenvalues of the tensor $\Omega_{ik}\Omega_{kj} + S_{ik}S_{kj}$, and $\lambda_1 < \lambda_2 < \lambda_3$.

In the current study, both vorticity magnitude and the λ_2 criterion are employed to visualize vortical structures. Figure 5 shows snapshots of the isovorticity surface at $|\omega| = 75{,}000\ \mathrm{s}^{-1}$ (Fig. 5a) and the iso-λ_2 surface at $\lambda_2 = -2.5 \times 10^9\ \mathrm{s}^{-2}$ (Fig. 5b) for $S = 0.44$ and 1.10. Because strong vorticity exists near the wall, the vorticity field in the region $r > 2$ cm is blanked to provide a clear view of the vortical structures inside the chamber. For the low-swirl-number case, a vortex spiral evolves from the shear layer originating at the backward-facing step due to the Kelvin–Helmholtz instabilities in both the axial and azimuthal directions. This vortical structure gyrates around the centerline and persists for about several turns before breaking up into small fragments. The spiral winds in the direction opposite to the main swirling flow, although the whole structure follows the main stream. For the high-swirl-number case, a spiral vortical structure is also observed. The structure, however, is much more complex because of the high centrifugal force. It spreads outward rapidly and soon breaks up into small-scale eddies. The vortical structures observed using the iso-λ_2 surface are more distinct than those observed using the isovorticity surface.

Figure 6 shows snapshots of the isovorticity and iso-λ_2 surfaces with the region $r > 1$ cm blanked. It is difficult to identify a distinct structure from the isovorticity surface for both the high- and low-swirl-number cases. However, the iso-λ_2 surface indicates the

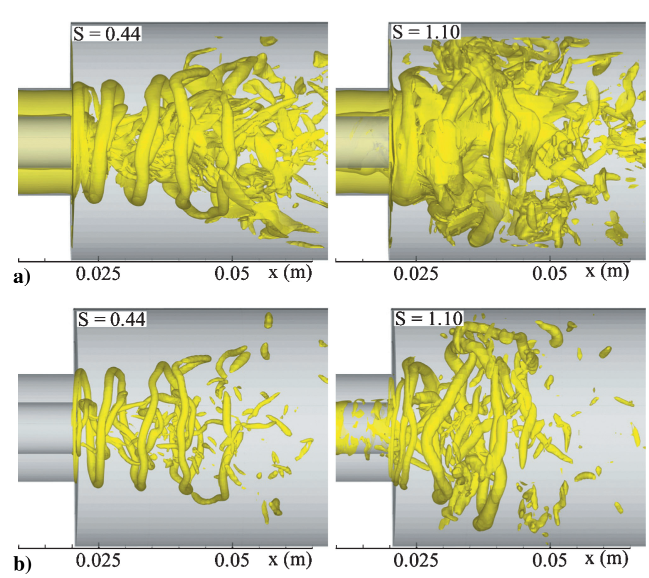

Fig. 5 Snapshots of a) isovorticity surface at $\omega = 75{,}000\ \mathrm{s}^{-1}$, $r > 0.02$ m blanked and b) iso-λ_2 surface at $\lambda_2 = -2.5 \times 10^9\ \mathrm{s}^{-2}$ for $S = 0.44$ and 1.10.

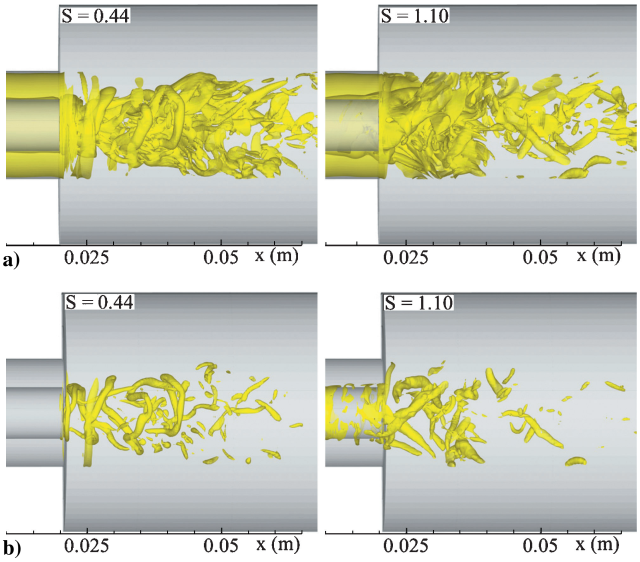

Fig. 6 Snapshots of a) isovorticity surface at $\omega = 75{,}000\ \mathrm{s}^{-1}$, $r > 0.01$ m blanked and b) iso-λ_2 surface at $\lambda_2 = -2.5 \times 10^9\ \mathrm{s}^{-2}$ for $S = 0.44$ and 1.10.

presence of a spiral vortex structure for $S = 0.44$ and a double helix vortex structure for $S = 1.10$, both originating from the shear layer near the centerbody.

The evolution of these spiral vortex structures can be regarded as a kind of vortex shedding process with well-defined frequencies, as indicated in Sec. IV. A. One may conjecture[5] that the vortical motions in the shear layers resonate with acoustic oscillations in the chamber. In the present configuration, two shear layers exist downstream of the rear-facing step and the centerbody. The axial momentum thickness θ_0 of each shear layer is estimated to be around 0.1 mm for the low-swirl-number case, based on the calculated mean velocity distribution. For the high-swirl-number case, the momentum thickness of the lower shear layer ($\approx$0.25 mm) differs from its upper counterpart ($\approx$0.05 mm) by a factor of five, due to its stronger swirl strength. A linear stability analysis has been carried out to provide more insight into the shear-layer instability phenomena for annular swirling flows in an open atomsphere.[35] The geometrical parameters were selected to match the current physical model. The effects of momentum thickness, swirl strength, and density and velocity ratios were studied systematically with different azimuthal wave numbers. The frequencies predicted to be most amplified are different for the two swirl numbers considered herein, mainly due to the disparity of the axial momentum thickness between the two cases. In addition, the predicted values are much higher than the vortex-shedding frequency, which corresponds to the frequency of the first tangential (1T) acoustic mode of motion in the present chamber. This observation indicates that the acoustic oscillation acts as a forced excitation to the system. The shear layers respond to the excitation by locking their shedding frequencies close to the forcing frequency.

C. Linear Acoustic Modal Analysis

Because the most problematic type of instability in a gas-turbine combustor involves the coupling between acoustic motion and flame dynamics, a prerequisite of any combustion instability research is the identification of acoustic eigenmodes in the combustor. Following the approach detailed in Refs. 36 and 37, a wave equation characterizing the acoustic instability can be derived as follows, subject to appropriate boundary conditions:

$$\nabla^2 p' - \frac{1}{\bar{c}^2}\frac{\partial^2 p'}{\partial t^2} = h(\bar{\boldsymbol{u}}, \bar{p}, u', p', q', \ldots) \tag{28}$$

where the prime denotes a fluctuating quantity and $\bar{c}$ the mean sound speed in the chamber. The source term h involves all of the volumetric and surface effects. If all of the source terms are ignored, the linearized version of Eq. (28) reduces to a Helmholtz equation,

Table 1 Oscillation frequencies predicted by linear acoustic modal analysis

Mode	Frequency, Hz
First longitudinal 1L	1,760
First tangential 1T	10,712
Second tangential 2T	17,820
First radial 1R	22,456

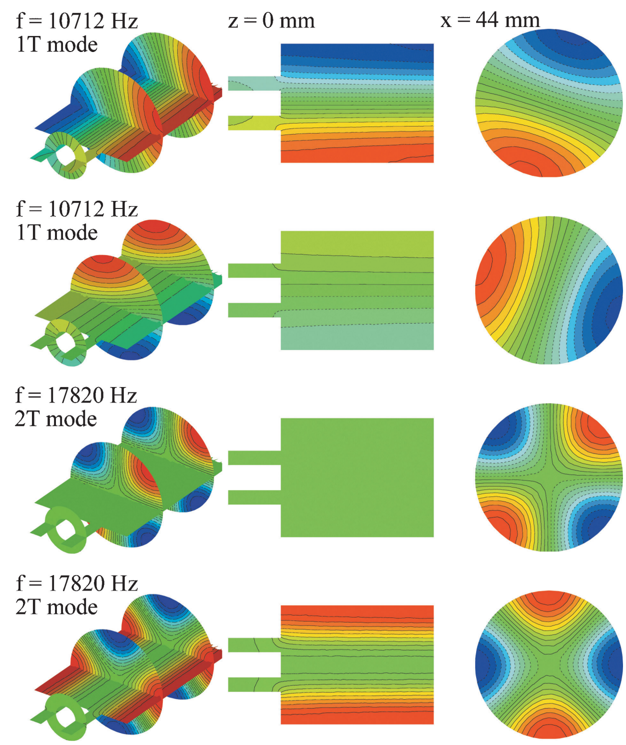

Fig. 7 Normalized acoustic pressure fields of 1T and 2T modes:——, positive values and - - - -, negative values.

which can be subsequently solved to determine the frequencies and spatial distributions of the normal acoustic modes of the system. An effective solution procedure,[37] which was recently constructed for problems involving complex configuration and nonuniform distributions of mean flow properties, is employed here for the acoustic modal analysis. The computational domain includes both the inlet annulus and the chamber. The mean flow properties were acquired from the LES database, and the choked exit nozzle is treated as an acoustically closed boundary. The acoustic impedance of the swirler was tuned to match the measured acoustic pressure distribution in the inlet annulus.[30] The predicted normal acoustic frequencies are summarized in Table 1. Note that, for each tangential acoustic mode, two solutions are found, and their spatial distributions shift away from each other in the circumferential direction. In the present cylindrical combustor configuration, the tangential acoustic wave can be expressed in the following general form:

$$p' = A(r, z)\cos(m\theta - \omega t + \phi) \tag{29}$$

where $A(r, z)$ is the amplitude, m an integer, θ the azimuthal coordinate, ω the radian frequency, and ϕ the phase angle determined by the initial condition. Equation (29) can be expanded as

$$p' = A(r, z)\cos(m\theta + \phi)\cos\omega t + A(r, z)\cos(m(\theta - \pi/2m) + \phi)\sin\omega t \tag{30}$$

The two terms on the right-hand side of Eq. (30) are also the solution of the Helmholtz equation, representing the standing transverse acoustic waves in the chamber. Figure 7 shows the calculated normalized acoustic pressure distributions of the 1T and second tangential (2T) modes. The circumferential phase shifts between the

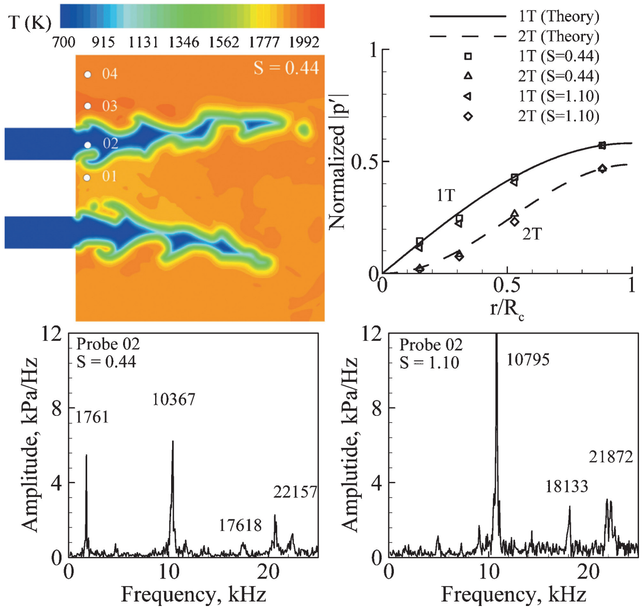

Fig. 8 Power spectral densities of pressure fluctuations immediately downstream of dump plane and spatial distributions of 1T and 2T modes of acoustic oscillation for $S = 0.44$ and 1.10.

two constituent wave motions for the 1T and 2T modes are 90 and 45 deg, respectively. This observation will be used along with the spectral and POD analyses to further identify the acoustic motions in the chamber, as will be shown later.

D. Spectral Analysis of Oscillatory Field

The oscillatory flowfield was carefully surveyed to provide direct insight into the driving mechanism for acoustic oscillations. A vast number of probes were employed to register the flow motions in various parts of the chamber. The fast Fourier transform (FFT) technique was used for the spectral analysis. Figure 8 shows the frequency contents of the pressure fluctuations immediately downstream of the dump plane. For $S = 0.44$, the dominant frequencies of 1761; 10,367; and 17,618 Hz correspond to the first longitudinal (1L), 1T, and 2T modes of acoustic motion in the chamber, respectively. The slight deviation from the prediction of the linear acoustic modal analysis results from the uncertainties in specifying the averaged speed of sound and the chamber length. Note that the experimental measurements[30] also indicate the existence of the second longitudinal (2L) mode at 3500 Hz. This mode, however, was suppressed in the present numerical study because the backpressure at the end of the computational domain was fixed at a prespecified value, a condition that prohibited the excitation of higher modes of longitudinal oscillations. For $S = 1.10$, the longitudinal wave disappears and the frequencies of the 1T and 2T modes shift slightly to 10,795 and 18,133 Hz, due to the change in the temperature field. Good agreement in the acoustic mode shape between the calculated and analytical results is obtained for both the 1T and 2T acoustic modes. Although the oscillation frequencies at 22,157 Hz for $S = 0.44$ and 21,872 Hz for $S = 0.11$ are close to the first radial (1R) acoustic mode (22,456 Hz), the mode shapes do not match well with the analytical result from classical acoustics and, thus, cannot be regarded as the 1R mode. This observation is also confirmed by the POD analysis to be discussed. The inlet swirl number exerts little influence on the acoustic frequencies, but plays a significant role in determining the wave amplitudes. The suppression of low-frequency oscillations in the high-swirl-number case may be attributed to the enhanced flame stiffness, which reduces the flame sensitivity to imposed disturbances.

E. Flame Surface and Heat Release Evolution

To understand the mutual coupling between the flame dynamics and flow oscillation, the total heat release and flame surface area

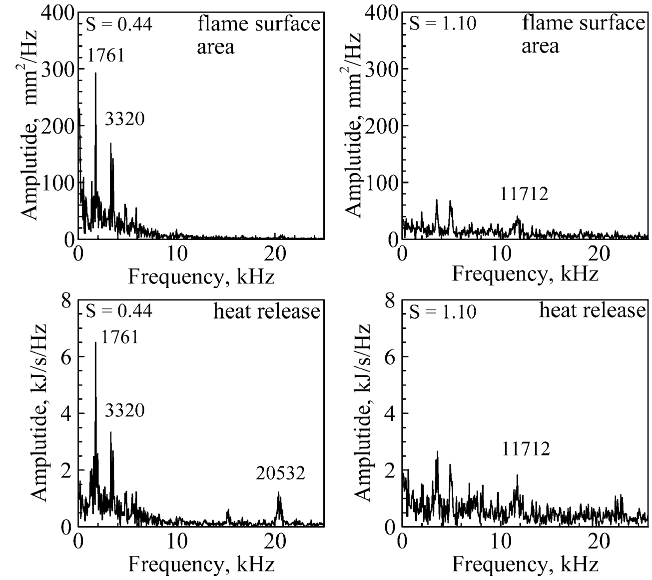

Fig. 9 Power spectral densities of total flame surface-area and heat-release fluctuations for $S = 0.44$ and 1.10.

were analyzed in the frequency domain. The overall heat release in the chamber can be obtained from

$$\dot{Q} = \rho_u \Delta h_f^0 S_T A \tag{31}$$

where ρ_u is the unburned gas density, S_T the subgrid turbulent flame speed, and Δh_f^0 the heat of reaction. A is the total filtered flame surface area, which can be evaluated numerically based on the level-set approach.[17,38,39]

Figure 9 shows the power spectral densities of the total filtered flame surface-area and heat-release fluctuations. At $S = 0.44$, a dominant mode exists at 1761 Hz in the flame surface oscillation, which corresponds to the 1L acoustic mode of the combustor. A higher harmonic at 3320 Hz is also found, approximately twice the frequency of the 1L mode. Although transverse acoustic motions including the 1T and 2T modes are observed, the flame surface-area oscillations do not exhibit such a high-frequency behavior. At $S = 1.10$, there is a small peak at 11,712 Hz near the 1T acoustic mode, but no corresponding 1L mode oscillation is found. The frequency content of the total heat-release fluctuations bears a close resemblance to that of flame surface-area variations. A small spike near the frequency of 20,532 Hz, however, is observed for $S = 0.44$, arising from the fluctuations in the subgrid turbulent flame speed S_T (Refs. 5 and 17). In light of the preceding observations, one can conclude that low-frequency acoustic perturbations exert a strong influence on the fluctuations of the total flame surface area and heat release. In contrast, high-frequency acoustic oscillations travel through the flame zone without significantly affecting the flame surface-area and heat-release variations, although they may impose a significant impact on the local flame propagation. The results agree well qualitatively with the prediction from a companion analytical analysis of flame response.[6] The calculated mean flame surface area and the root mean square of the fluctuating quantity for the high-swirl-number case are much smaller than those of the low-swirl-number case. However, owing to the increased turbulence intensity and the ensuing enhancement of the flame speed in the high-swirl-number case, the mean heat-release rate and the associated fluctuation are very close in these two cases.

F. Acoustics and Flame Interaction

Figure 10 shows the temporal evolution of the isothermal surface at $T = 1700$ K over one cycle of the 1L mode of acoustic oscillation at $S = 0.44$. Such information provides a good insight into the flame development because the adiabatic flame temperature is 1902 K in the present case. The phase angle θ is referenced to the 1L acoustic pressure at the chamber head end. The entire process is dictated by the cold-flow entrainment into and mixing with hot

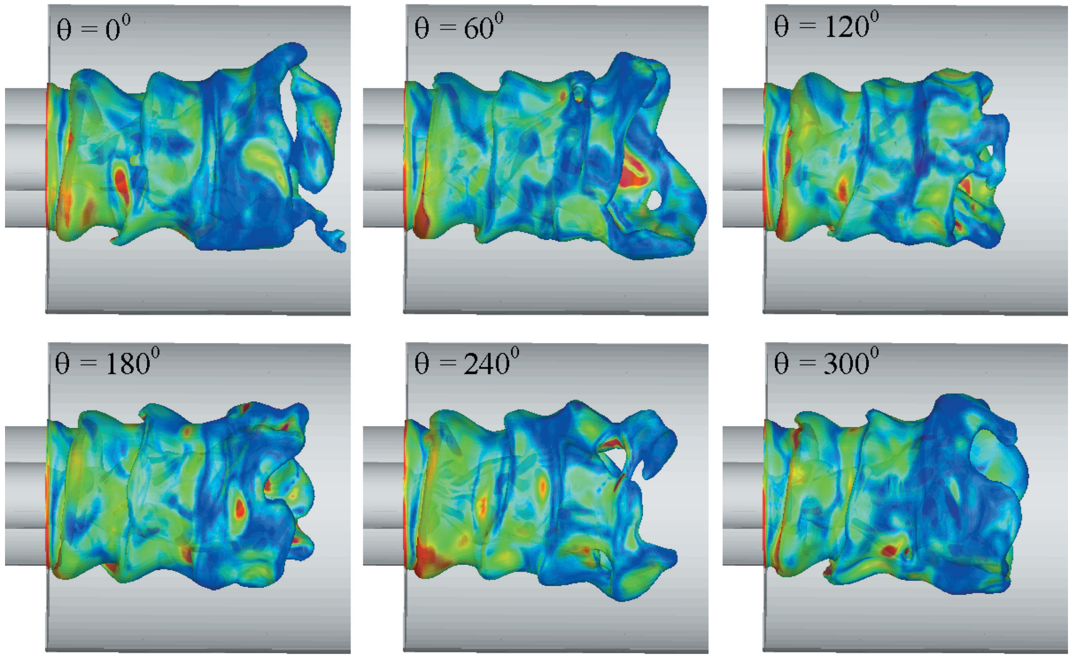

Fig. 10 Temporal evolution of isothermal surface at $T = 1700$ K (colored by vorticity magnitude) over one cycle of 1L mode of oscillation for $S = 0.44$.

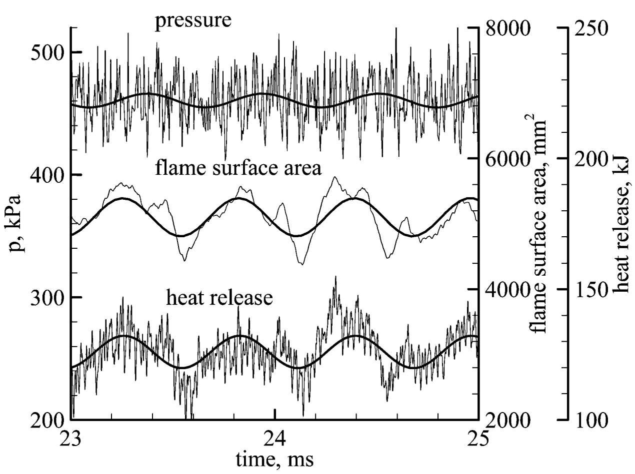

Fig. 11 Time histories of pressure immediately downstream of dump plane (top), total flame surface area (middle), and rate of total heat release (bottom) for $S = 0.44$:——, extracted 1L oscillations.

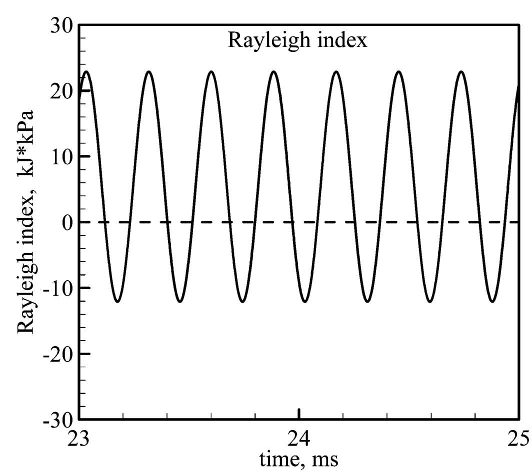

Fig. 12 Time evolution of instantaneous Rayleigh index, $p^a \cdot \dot{Q}^a(t)$, over entire chamber for 1L mode of oscillation for $S = 0.44$.

gases in the vortical structures in the flame zone. Figure 11 shows the time histories of the pressure immediately downstream of the dump plane (top), the total flame surface area (middle), and the rate of heat release (bottom). These signals involve a wide range of frequencies corresponding to turbulent-flow and acoustic oscillations. The extracted 1L oscillations (denoted by the thick black lines) of these quantities are also plotted for clarity. The flame surface-area variation can be elucidated by considering its interaction with the local oscillatory flowfield. It lags behind the pressure oscillation by 76 deg. During the period from $\theta = -166$ deg ($t = 24.09$ ms) to 14 deg ($t = 24.38$ ms), a relatively lower pressure field exists near the dump plane, facilitating the delivery of the fresh reactants into the chamber. Intensive heat release then occurs after a short fluid-mixing and chemical-induction time. The resultant flow expansion pushes the flame outward and causes the flame surface area to increase from a trough to a crest. Unburned mixture fragments may be shattered away from the main stream and generate local hot spots when convected downstream. During the period from $\theta = 14$ deg ($t = 24.38$ ms) to 194 deg ($t = 24.66$ ms), the relatively higher pressure near the

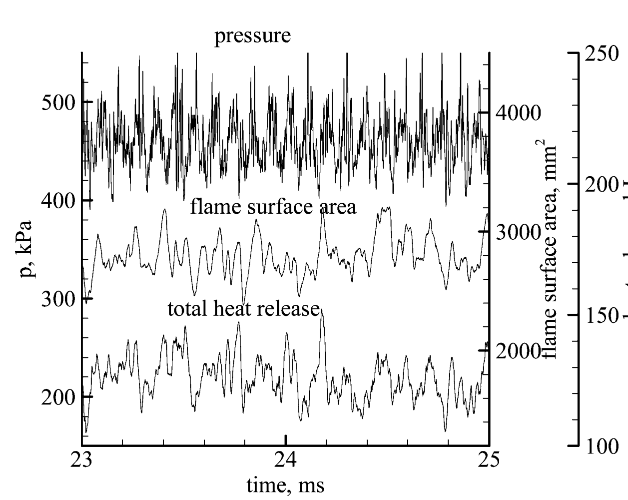

Fig. 13 Time histories of pressure immediately downstream of dump plane (top), total flame surface area (middle), and rate of total heat release (bottom) for $S = 1.10$.

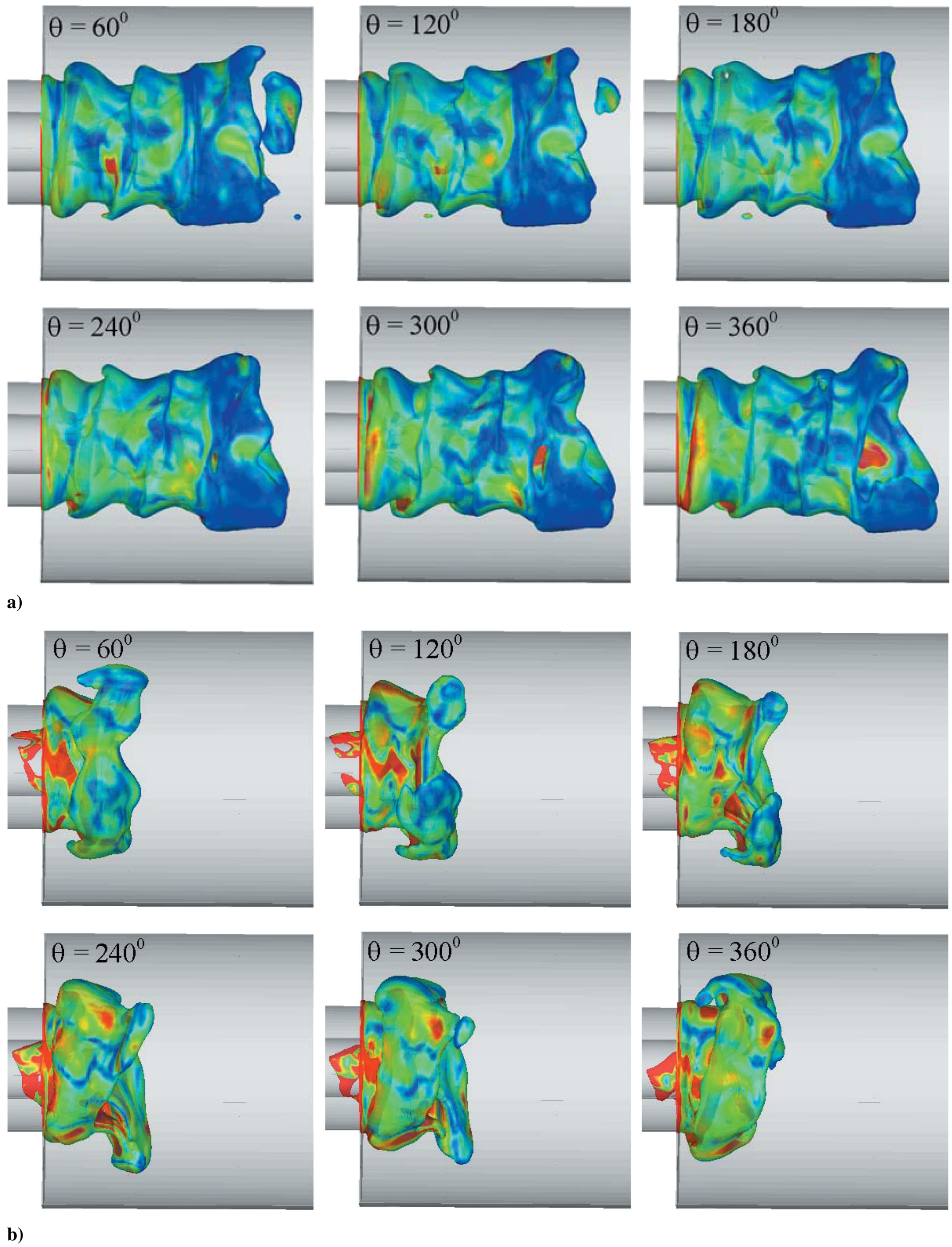

Fig. 14 Temporal evolution of isothermal surface at $T = 1700$ K (colored by vorticity magnitude) over one cycle of 1T mode of oscillation for a) $S = 0.44$ and b) $S = 1.10$.

dump plane prevents the fresh reactants from traveling downstream into the chamber. The flame zone is, thus, reduced and becomes a little more compact. The same process then repeats for another cycle of oscillation. Figure 11 also shows that the heat-release and flame surface-area fluctuations are nearly in phase. The former only lags behind the flame surface-area oscillation by 4 deg. Figure 12 shows the time evolution of the instantaneous Rayleigh index, $p^a \cdot \dot{Q}^a(t)$, over the entire chamber for the 1L mode oscillation. This parameter is positive over most of the time period, suggesting the excitation and sustenance of the 1L oscillations by the flame. For the high-swirl-number case with $S = 1.10$, no obvious 1L oscillation can be observed, as shown in Fig. 13.

Figure 14 shows the temporal evolution of the isothermal surface at $T = 1700$ K over one cycle of the 1T mode of acoustic oscillation. For both swirl numbers, new vortices are produced at the edge of the backward-facing step and bulge the flame front. They continue to distort the flame or even produce separated flame pockets when traveling downstream, although for the high-swirl-number case this process is less apparent due to the reduced flame length. This kind of interaction between the vortex and the flame is also observed downstream of the centerbody. As the swirl number increases, the flame anchored by the center recirculating flow may propagate upstream periodically and cause flame flashback. Two mechanisms have been identified for the occurrence of flame flashback.[16] The first involves flame propagation in the boundary layer along a solid wall where the local velocity diminishes toward the surface. The second is associated with flow reversal, which usually results from vortical motions or acoustic oscillations. In the current case, flashback is closely linked to the strong reverse flow in the center recirculation zone. The swirl is so strong that it sometimes causes the center recirculating flow to enter into the inlet annulus. As a consequence, the flame attached to the centerbody travels upstream and flashback occurs.

G. Proper Orthogonal Decomposition Analysis

The combustion dynamics are further explored using the POD technique. The POD method is an empirical mathematical technique capable of extracting dynamically significant structures from the flowfield of concern. This method has been extensively employed to study nonreacting flows.[15,28,40–45] Its application to research in combustion dynamics has recently received some attention.[46,47] Most of the existing studies, however, adopted the techniques developed for incompressible flows, which do not consider the effects of fluid compressibility. In the current work, we present a method for applying the POD technique to compressible flows by introducing an acoustic-energy-based inner product, as will be shown hereafter.

A rigorous description of the POD method can be found by Berkooz et al.[48] and Cordier and Bergmann.[49] It will be briefly reviewed here. The POD analysis takes as input an ensemble of instantaneous realizations or snapshots, which is obtained from physical experiments or numerical simulations, and extracts base functions optimal for the representation of the data. More precisely, if we consider a collection of observations $\boldsymbol{q}(\boldsymbol{x}, t_m)$ obtained at M different time steps t_m over a spatial domain of interest Ω, the POD method attempts to determine a set of orthogonal base functions $\varphi^{(n)}(\boldsymbol{x})$, $n = 1, \ldots, M$, such that the projection of $\boldsymbol{q}(\boldsymbol{x}, t_m)$ onto the base functions,

$$\hat{\boldsymbol{q}}(\boldsymbol{x}, t_m) = \sum_{n=1}^{M} a^{(n)}(t_m)\varphi^{(n)}(\boldsymbol{x}) \tag{32}$$

has the smallest error, defined as $\langle \|\boldsymbol{q} - \hat{\boldsymbol{q}}\|^2 \rangle$, where $a^{(n)}(t_m)$ is the expansion coefficient. The symbol $\langle\ \rangle$ denotes a time or ensemble average, and $\|\cdot\|$ the norm associated with the inner product $(,)$ in the Hilbert space of square integral functions.

Based on the calculus of variations, the POD modes φ can be determined by the following integral eigenvalue equation:

$$\int_\Omega R_{i,j}(\boldsymbol{x}, \boldsymbol{x}')\varphi_j^{(n)}(\boldsymbol{x}')\,\mathrm{d}\boldsymbol{x}' = \lambda^{(n)}\varphi_i^{(n)}(\boldsymbol{x}) \tag{33}$$

where $R_{i,j}(\boldsymbol{x}, \boldsymbol{x}')$ is a two-point spatial correlation tensor. For a standard inner product, it can be written as

$$R_{i,j}(\boldsymbol{x}, \boldsymbol{x}') = \langle \boldsymbol{q}_i(\boldsymbol{x})\boldsymbol{q}_j(\boldsymbol{x}')\rangle \tag{34}$$

To compute POD modes, we first need to make an appropriate choice of a vector-valued flow variable $\boldsymbol{q}(\boldsymbol{x}, t)$ and define a suitable inner product on the configuration space. For an incompressible system, the flow variable is usually chosen as the velocity with $\boldsymbol{q} = (u, v, w)$, and the standard inner product gives

$$(\boldsymbol{q}_1, \boldsymbol{q}_2) = \int_\Omega (u_1u_2 + v_1v_2 + w_1w_2)\,\mathrm{d}\boldsymbol{x} \tag{35}$$

The induced norm

$$\|\boldsymbol{q}\|^2 = \int_\Omega (u^2 + v^2 + w^2)\,\mathrm{d}\boldsymbol{x}$$

corresponds to the total kinetic energy over the domain Ω of concern. The mean kinetic energy of the flowfield is equal to the sum of the eigenvalues divided by two, as shown here:

$$\begin{aligned} E &= \frac{1}{2}\int_\Omega \langle u^2 + v^2 + w^2\rangle\,\mathrm{d}\boldsymbol{x} = \frac{1}{2}\int_\Omega R_{i,i}(\boldsymbol{x}, \boldsymbol{x})\,\mathrm{d}\boldsymbol{x} \\ &= \frac{1}{2}\int_\Omega \sum_{n=1}^{M} \lambda^{(n)}\varphi_i^{(n)}(\boldsymbol{x})\varphi_i^{(n)}(\boldsymbol{x})\,\mathrm{d}\boldsymbol{x} = \frac{1}{2}\sum_{n=1}^{M}\lambda^{(n)} \end{aligned} \tag{36}$$

Each eigenvalue represents the portion of the energy associated with the corresponding eigenfunction.

For a compressible system, the flow-variable vector should include a thermodynamic parameter, such as density and pressure, characterizing the effects of fluid compressibility. The best choices of the inner product and norm, however, are not obvious. The standard inner product may not be a sensible choice, according to Rowley et al.[50] For example, if we select the baseline flow variables as $\boldsymbol{q} = (\rho, u, v, w, p)$, the standard inner product leads to

$$(\boldsymbol{q}_1, \boldsymbol{q}_2) = \int_\Omega (\rho_1\rho_2 + u_1u_2 + v_1v_2 + w_1w_2 + p_1p_2)\,\mathrm{d}\boldsymbol{x} \tag{37}$$

which does not make dimensional sense and carries little physical significance. Rowley et al.[50] proposed the flow variables as $\boldsymbol{q} = (u, v, w, c)$, with c being the local speed of sound, and defined a family of inner products as

$$(\boldsymbol{q}_1, \boldsymbol{q}_2) = \int_\Omega \left(u_1u_2 + v_1v_2 + w_1w_2 + \frac{2\alpha}{\gamma - 1}c_1c_2\right)\mathrm{d}\boldsymbol{x} \tag{38}$$

where γ is the ratio of specific heats and α a weighting parameter. The induced norm corresponds to either the specific stagnation enthalpy for $\alpha = 1$ or the specific stagnation energy for $\alpha = 1/\gamma$, respectively.

In the current study, because we are primarily concerned with acoustic oscillations, the flow variables based on the fluctuating quantities are preferred.[51] A family of new norms accounting for the acoustic energy is introduced. The flow-variable vector is defined as $\boldsymbol{q}' = (u', v', w', p')$, and a new inner product is proposed as

$$(\boldsymbol{q}_1', \boldsymbol{q}_2') = \int_\Omega \left[\alpha_1(u_1'u_2' + v_1'v_2' + w_1'w_2') + \alpha_2\frac{p_1'p_2'}{\bar{\rho}^2\bar{c}^2}\right]\mathrm{d}\boldsymbol{x} \tag{39}$$

where α_1 and α_2 are two weighting parameters. If $\alpha_1 = 1$ and $\alpha_2 = 1$, the induced norm

$$\int_\Omega \left(u'^2 + v'^2 + w'^2 + \frac{p'^2}{\bar{\rho}^2\bar{c}^2}\right)\mathrm{d}\boldsymbol{x}$$

is twice the total energy of the entire oscillatory flowfield. The induced norm corresponds to the kinetic energy of unsteady motions if $\alpha_1 = 1$ and $\alpha_2 = 0$ and to the potential energy if $\alpha_1 = 0$ and $\alpha_2 = 1$.

The LES database for the POD analysis contains a total of 200 data sets or snapshots for each swirl number. The spatial domain of concern only includes the upstream portion of the computational domain and has 2.0 million grid points. The time interval at which the snapshots were sampled was 6.0 μs, compared with the time step of 0.03 μs employed in the numerical simulations. Thus, the total time span was approximately 2.1 and 12.5 times of the 1L and 1T acoustic oscillation periods. The size of each database is around 30 GB, so that extensive computer storage space is required for POD analysis.

Figure 15 shows the energy distributions of the POD modes based on the acoustic pressure fields for two different swirl numbers. In the low-swirl-number case with $S = 0.44$, the first two modes have almost the same energy level, that is, 31.28 and 29.14%, and collectively capture more than 60% of the total energy of the oscillatory flowfield. A similar observation is made for the high-swirl-number case with $S = 1.10$, where the first and second modes represent 37.22 and 34.16% of the total energy, respectively. In both cases, the first 16 modes account for more than 80% of the total energy. The frequency spectra of the time-varying coefficients, $a^{(n)}(t)$, of the first

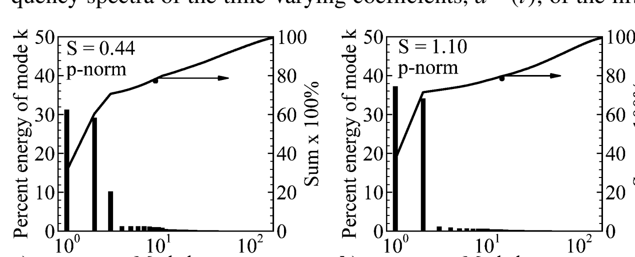

Fig. 15 Energy distributions of POD modes based on acoustic pressure fields for a) $S = 0.44$ and b) $S = 1.10$.

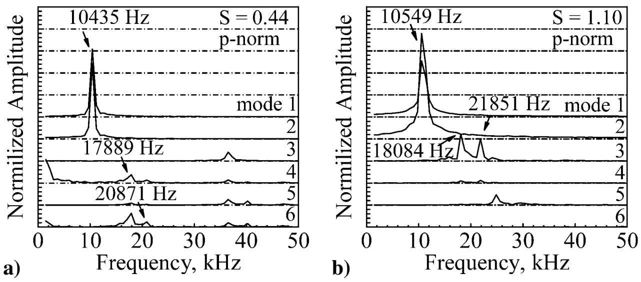

Fig. 16 Frequency spectra of time-varying coefficients of first six POD modes based on acoustic pressure fields for a) $S = 0.44$ and b) $S = 1.10$.

six POD modes are shown in Fig. 16. For the low-swirl-number case, the dominant frequencies of 10,435 Hz for the first two modes and 17,889 Hz for the fourth and sixth modes correspond to the 1T and 2T acoustic modes in the chamber, respectively. The same phenomenon occurs with the high swirl number, with the first two modes and modes 3 and 4 associated with the 1T and 2T acoustic mode of oscillations, respectively, although the dominant frequencies shift slightly due to the variation in the flowfield. For both swirl numbers, the 1L acoustic mode is not observed. This may be attributed to the relatively short time span of the database compared with the 1L acoustic oscillation period.

Figure 17 shows the spatial distributions of the fluctuating pressure field for the first six POD modes for $S = 0.44$. The first two

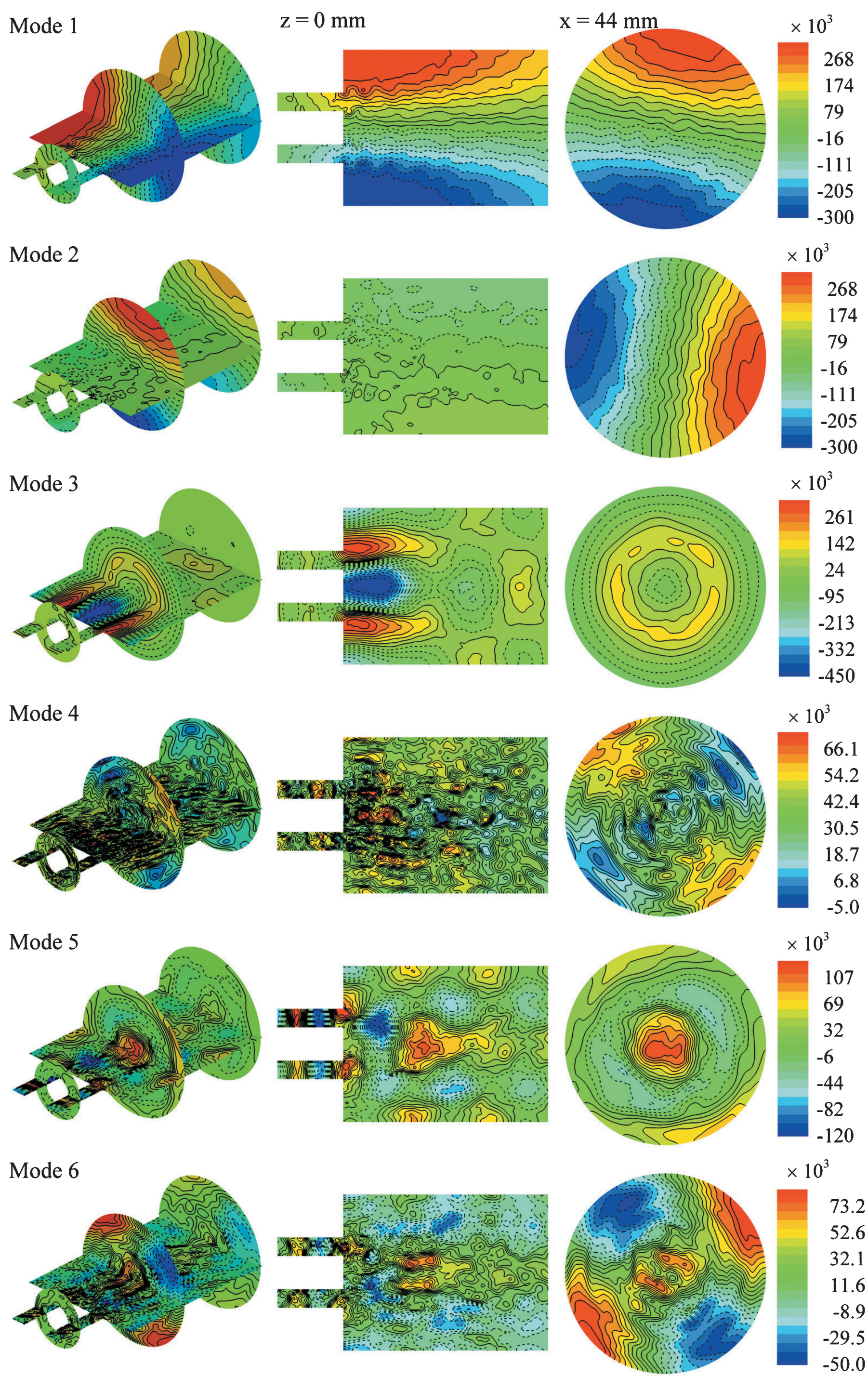

Fig. 17 Spatial distributions of first six POD modes of fluctuating pressure field for $S = 0.44$.

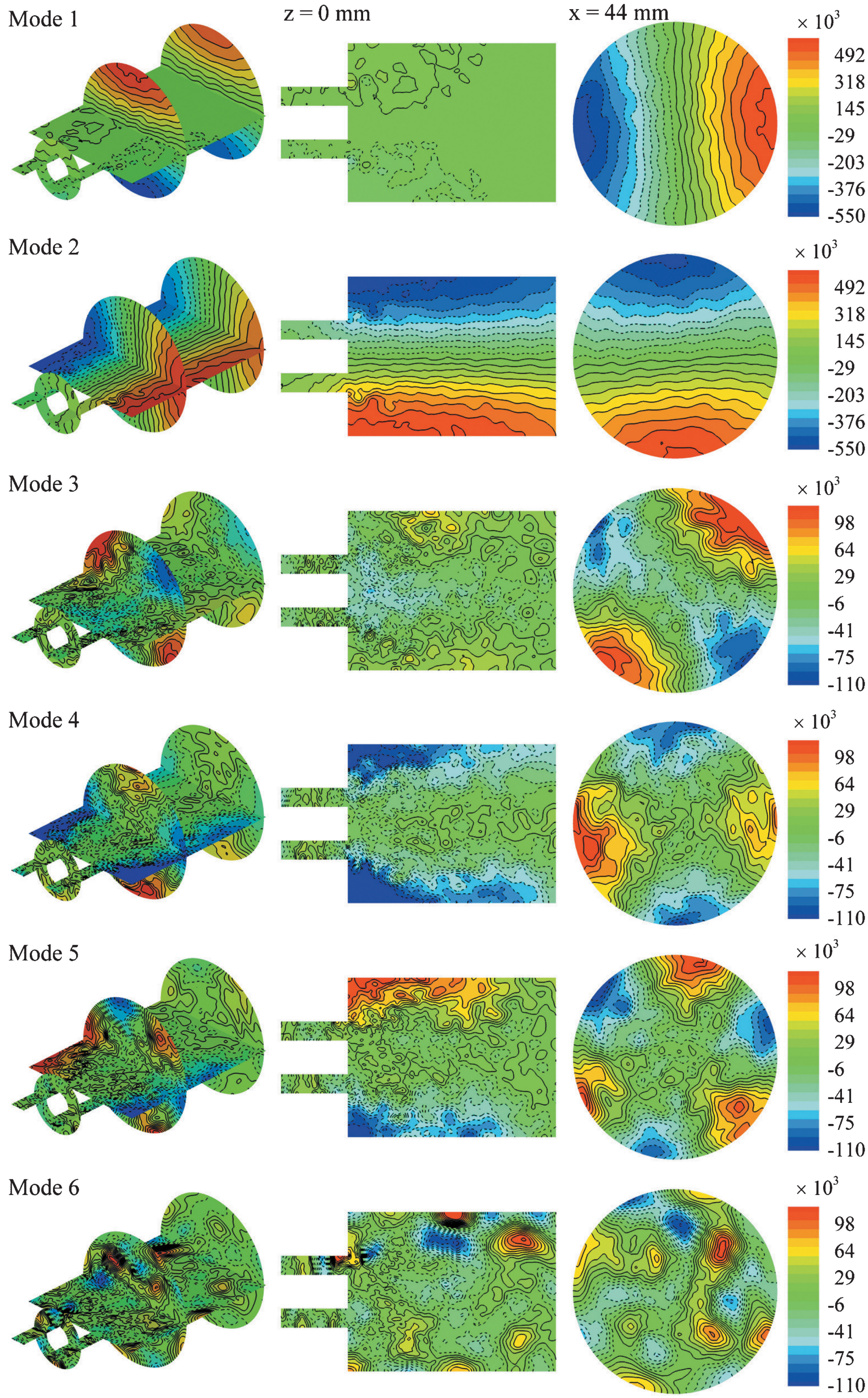

Fig. 18 Spatial distributions of first six POD modes of fluctuating pressure field for $S = 1.10$.

modes, shifted from each other by 90 deg in the azimuthal direction, are almost identical to the 1T acoustic mode shapes shown in Fig. 7. The wave motion is most intensive near the dump plane, where heat release takes place, and gradually decays downstream along the length of the chamber. Mode 3 has an axisymmetric distribution, with its strongest oscillations in the shear layer and downstream of the centerbody. Modes 4 and 6 closely resemble the 2T acoustic mode. Their mode shapes differ from each other by 45 deg in the azimuthal direction. Mode 5 has a more complex structure and does not correspond to a normal acoustic mode shape.

Figure 18 shows the first six POD mode shapes of the fluctuating pressure field for $S = 1.10$. Similarly to the low-swirl-number case, the first two modes match closely the 1T acoustic structure with an azimuthal phase shift of 90 deg between them. Modes 3 and 4 correspond to the 2T acoustic mode and have an intermode phase shift of 45 deg in the azimuthal direction. The higher modes have much more intricate distributions but carry much less energy. All of these results indicate that the POD method is able to capture the detailed acoustic wave structure in the chamber. In fact, it is well established[52,53] that the optimal base functions obtained by the POD method consist of the Fourier modes in the homogeneous (periodic) coordinate directions, that is, in the azimuthal direction in the current case.

Figure 19 shows the energy distributions of the POD modes for the total acoustic energy fields, defined by Eq. (39) with $\alpha_1 = 1$ and $\alpha_2 = 1$, for two different swirl numbers. Although the first two modes still dominate, they only capture about 42 and 50% of the total energy of the oscillatory flowfields for $S = 0.44$ and 1.10, respectively. The frequency spectra of the time-varying coefficient, $a^{(n)}(t)$, of the POD modes were also examined (not shown). For both swirl numbers, the 2T acoustic mode was not observed, although it was seen in the acoustic potential energy field shown in Fig. 16. The POD method based on the acoustic potential energy appears to be more effective in capturing acoustic motions and will be used in the subsequent analysis.

H. Energy Exchange Mechanisms in Oscillatory Flowfield

The instantaneous flowfield can be reconstructed from the POD modes by means of Eq. (32). Such a procedure allows us to examine how the various POD modes contribute to the instantaneous events occurring in the chamber. Figure 20 shows the time histories of the pressure and axial velocity u_x immediately downstream of the dump plane, with $r = 7.5$ mm for $S = 0.44$. The signals reconstructed, respectively, from the first 2 and first 12 modes are also included for comparison. The flowfield can be reasonably recovered with 12 modes and matches the original data well. The first two modes, however, unambiguously capture the dominant flow motions in a complex turbulent flowfield through proper orthogonal decomposition. A similar observation were made for the high-swirl-number case with $S = 1.10$.

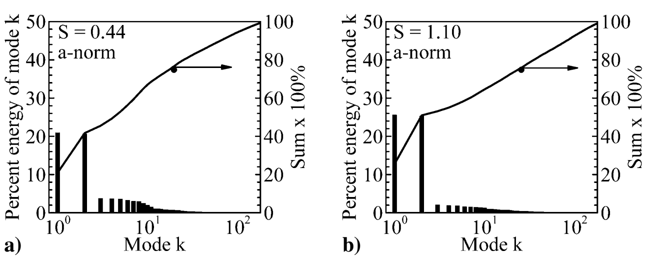

Fig. 19 Energy distributions of POD modes for total acoustic energy fields for a) $S = 0.44$ and b) $S = 1.10$.

Figure 21 shows the temporal evolution of the reconstructed pressure field based on the first two POD modes on a transverse plane, $x = 32$ mm, over one cycle of the 1T mode of oscillation for two different swirl numbers. The spinning 1T acoustic wave motions in the azimuthal direction are clearly observed for both cases. The phenomenon can be mathematically attributed to the existence of two equal-valued eigenvalues corresponding to the 1T acoustic oscillation. According to Aubry et al.,[54] the near degeneracy of the eigenvalue problem defined by Eq. (33) is a result of the presence of traveling waves (or structures) in the flowfield, which is also related to the spatio-temporal symmetry of the system. This kind of behavior is encountered in many POD applications.[49,55,56] Figure 22 shows the temporal evolution of the reconstructed heat-release field based on the first two modes on the same transverse plane over one cycle of the 1T mode of oscillation. The helical structures in the flame development are evidenced in the shear-layer region.

Because the acoustic, that is, periodic, field is dominated by the 1T oscillation and can be well characterized by the first two POD modes, the entire fluctuating flowfield can be expressed as the sum of periodic and turbulent components as follows:

$$\hat{\boldsymbol{q}}'(\boldsymbol{x}, t_m) = a^{(1)}(t_m)\varphi^{(1)}(\boldsymbol{x}) + a^{(2)}(t_m)\varphi^{(2)}(\boldsymbol{x}) + \sum_{n=3}^{M} a^{(n)}(t_m)\varphi^{(n)}(\boldsymbol{x}) = \hat{\boldsymbol{q}}^a(\boldsymbol{x}, t_m) + \hat{\boldsymbol{q}}^t(\boldsymbol{x}, t_m) \tag{40}$$

This representation provides us with a convenient way to analyze the mechanisms of energy transfer among various constituent flowfields in the combustor, as formulated in Sec. II. Figures 23 and 24 show the distributions of $Ra = \overline{p^a \dot{q}^a}(\gamma - 1)/\gamma \bar{p}$, $R_{\rho uu} = \overline{\rho u_i^a u_j^a} \partial \bar{u}_i / \partial x_j$, and $R_{pu} = \overline{p^a \partial u_j^a / \partial x_j}$ for the 1T acoustic oscillation on a longitudinal and a transverse plane for the two different swirl numbers, respectively. Here the periodic components of the fluctuating flowfield, p^a, $\dot{q}^a$, and u_i^a are obtained using Eq. (40) through the POD method. The Rayleigh parameter Ra, which appears in Eqs. (23) and (24), represents the coupling between oscillatory heat release and pressure. It provides a qualitative measure of the extent to which unsteady heat

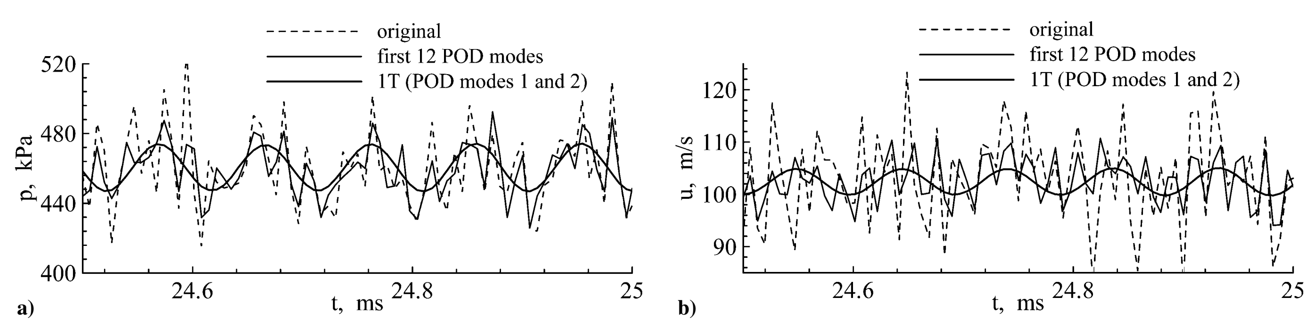

Fig. 20 Time histories of a) pressure and b) axial velocity immediately downstream of dump plane, $r = 7.5$ mm, for $S = 0.44$.

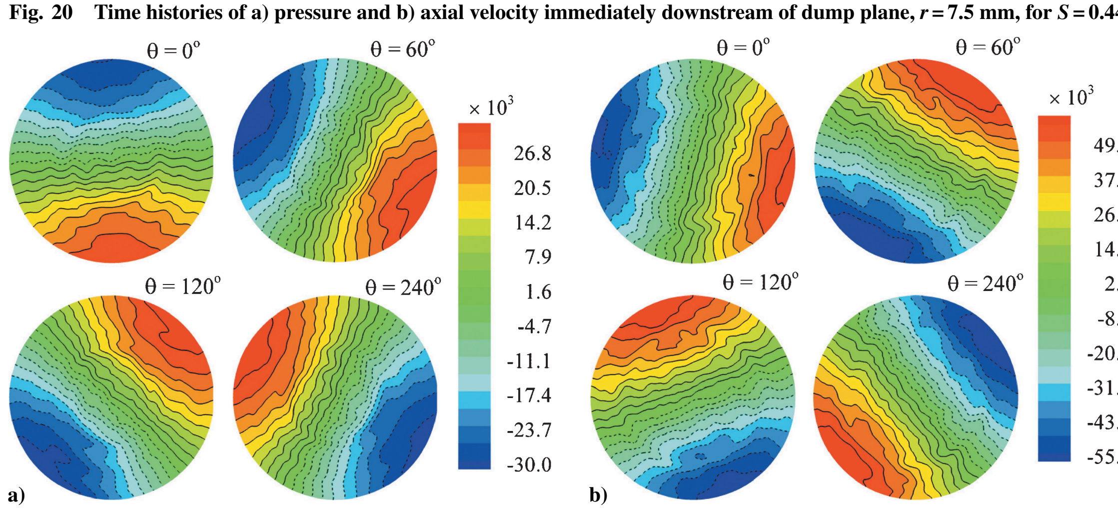

Fig. 21 Temporal evolution of pressure field reconstructed from first two POD modes on a transverse plane, $x = 32$ mm, over one cycle of 1T mode of oscillation for a) low swirl number $S = 0.44$ and b) high swirl number $S = 1.10$.

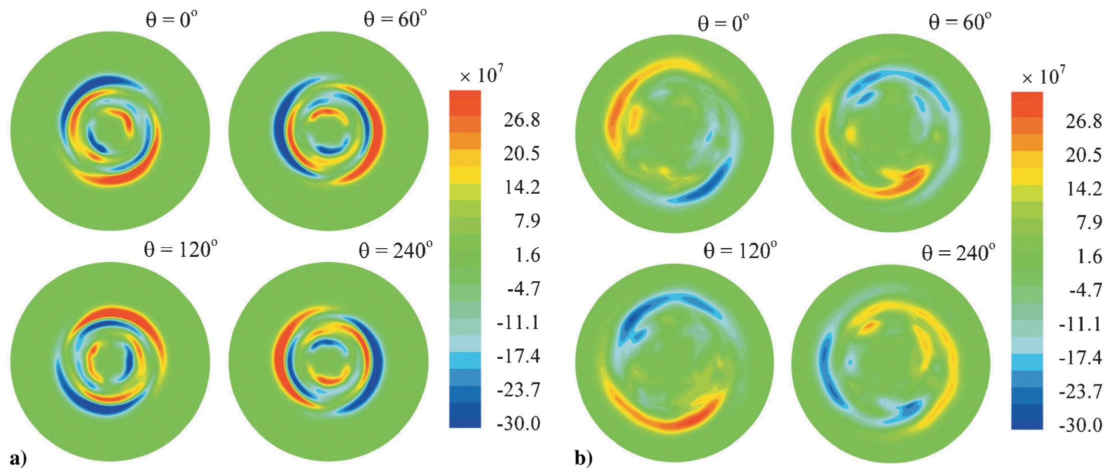

Fig. 22 Temporal evolution of heat release field reconstructed from first two POD modes on a transverse plane, $x = 32$ mm, over one cycle of 1T mode of oscillation for a) low swirl number $S = 0.44$ and b) high swirl number $S = 1.10$.

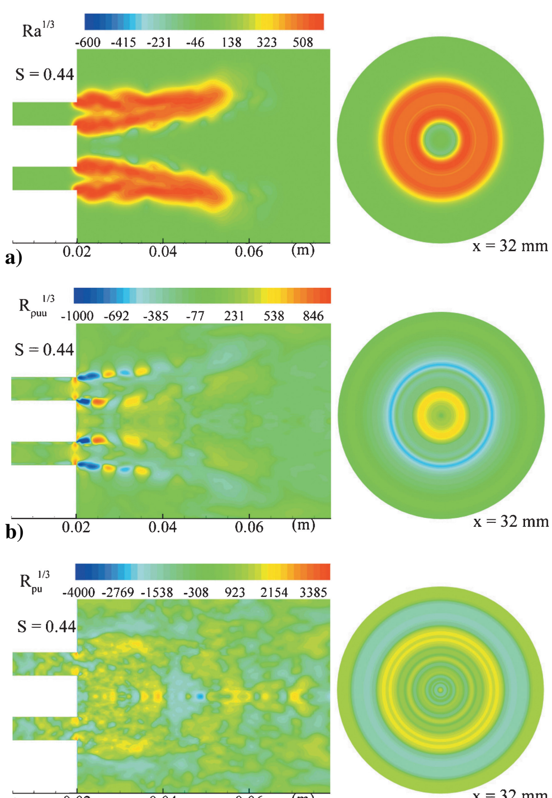

Fig. 23 Distributions of a) $Ra = \overline{p^a \dot{q}^a}(\gamma - 1)/\gamma\bar{p}$, b) $R_{\rho uu} = \overline{\rho u_i^a u_j^a}\partial\bar{u}_i/\partial x_j$, and c) $R_{pu} = \overline{p^a \partial u_j^a/\partial x_j}$ for 1T mode of oscillation on x–r and r–θ planes for $S = 0.44$.

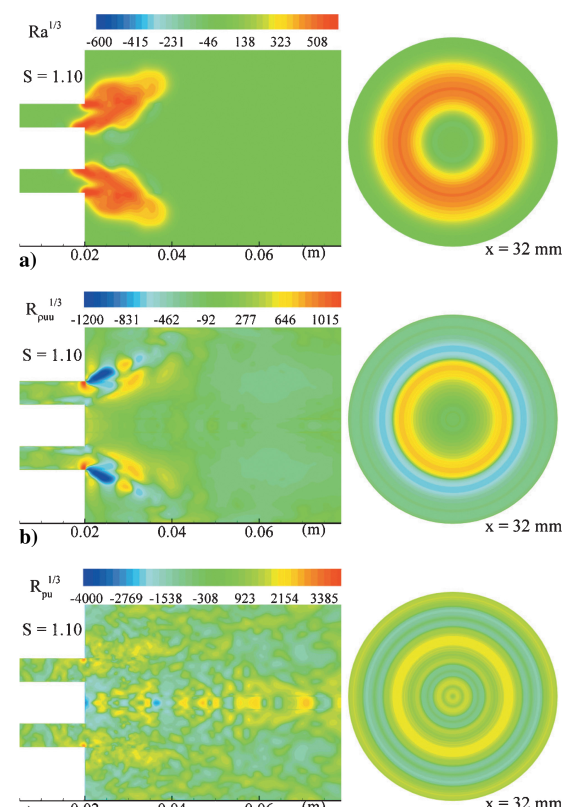

Fig. 24 Distributions of a) $Ra = \overline{p^a \dot{q}^a}(\gamma - 1)/\gamma\bar{p}$, b) $R_{\rho uu} = \overline{\rho u_i^a u_j^a}\partial\bar{u}_i/\partial x_j$, and c) $R_{pu} = \overline{p^a \partial u_j^a/\partial x_j}$ for 1T mode of oscillation on x–r and r–θ planes for $S = 1.10$.

release drives or suppresses flow oscillations. The acoustic motion is amplified if $Ra > 0$ or damped out if $Ra < 0$. For both swirl numbers, a wavy distribution of Ra takes place along the flame front. The Rayleigh parameter has a positive value in much of the flame zone. The 1T acoustic oscillation is favorably correlated with the unsteady heat release and extracts energy from chemical reactions. In a previous work,[5] the conventional decomposition technique, in which flow variables are expressed as the sum of mean and fluctuating quantities, was applied to explore the coupling between oscillatory heat release and pressure for the case with a swirl number $S = 0.76$. The spatial distribution of the correlation between fluctuating pressure and heat release, defined as the Rayleigh parameter in Ref. 5, was presented. An array of asymmetrical dipoles, that is, a combination of monopoles and dipoles, was observed downstream of the edges of the backward-facing step and the centerbody, with an overwhelming positive value in the flame zone in spite of the presence of strong background turbulent motions. The result demonstrated that coherent structures are indeed a dominant feature in the flowfield of concern. This is consistent with the observations in the current study. The difference between conventional and triple-decomposition techniques lies in that the latter allows periodic motions to be clearly separated from random turbulent motions. Thus, we can treat periodic motions more specifically and analyze the driving mechanisms of a particular mode of flow oscillation more accurately, for example, the 1T mode in the current study. The parameter $R_{\rho uu}$, which can be found in Eqs. (20) and (21), characterizes the kinetic energy exchange between the mean and oscillatory flowfields. If $R_{\rho uu}$ is negative, energy is transferred from the mean to the oscillatory flowfield. A well-organized distribution of $R_{\rho uu}$ is observed in the shear layers downstream of the backward-facing step and the centerbody. These structures, aligned with regions with alternate positive and negative values, exhibit strong interactions between the mean and periodic flowfields. The parameter R_{pu}, appearing in Eqs. (21) and (23), stands for the exchange between the kinetic and potential energies of flow oscillations. Such an energy exchange process occurs almost everywhere in the chamber, but much more vigorously in the flame zone and the central toroidal recirculation region.

V. Summary

A systematic data analysis has been conducted to explore the underlying mechanisms responsible for driving unsteady motions in gas-turbine systems, based on the time-resolved data obtained from an LES study. As a specific example, the detailed flow evolution and flame dynamics in a lean-premixed swirl-stabilized combustor operating under unstable conditions was carefully examined. Various data processing and analysis methods were developed and implemented to provide direct insights into the complex flowfields.

The interplay of mean, periodic, and turbulent flow motions in turbulent reacting flows, as well as their collective interactions with chemical heat release, were explored using a triple-decomposition technique. The oscillatory motions acquire energy through several different pathways. They may extract energy from the mean flowfield and chemical reactions, exchange energy with background turbulent motion, or be dissipated into thermal energy through viscous damping.

Results from the spectral analysis of the oscillatory flowfield and linear acoustic modal analysis indicate the presence of a variety of acoustic modes in the chamber, including both longitudinal and tangential modes of oscillations. Transverse acoustic waves prevail in the present combustor for a wide range of swirl numbers, where longitudinal modes are present only in cases with weak swirl. Low-frequency flow oscillations exert a strong influence on the fluctuations of the total flame surface area and heat release. In contrast, high-frequency flow oscillations have a limited effect on the global behavior of the flame dynamics. Both vorticity magnitude and the λ_2 criterion are employed to characterize the vortical flow development. It was found that acoustic oscillation acts on the system as a forced excitation. The shear layers respond to this excitation by locking their vortex shedding frequencies to the acoustic forcing frequency.

The POD technique is employed along with a triple-decomposition method to further examine the combustion dynamics. A method for applying the POD technique to compressible flows is developed by introducing an acoustic-energy-based inner product. The transverse acoustic field can be appropriately represented by the first two POD modes, which capture the majority of the acoustic energy associated with oscillatory flow motions. The entire flowfield can be effectively reconstructed using the POD techniques, rendering the investigation of various energy-transfer mechanisms in the flowfield a manageable task.

Acknowledgments

The work reported in this paper was sponsored in part by the Office of Naval Research under Grant N00014-96-1-0405, in part by the NASA Glenn Research Center under Grant NAG 3-2151, and in part by the Air Force Office of Scientific Research under Grant F49620-99-0290. The support and encouragement provided by Gabriel Roy and Kevin Breisacher are gratefully acknowledged. The authors also thank Danning You for her help with the acoustic modal analysis.

References

[1] Lieuwen, T., and McManus, K., "Combustion Dynamics in Lean-Premixed Prevaporized Gas Turbine," *Journal of Propulsion and Power*, Vol. 19, 2003, p. 721.

[2] Lieuwen, T., and Yang, V. (eds.), *Combustion Instabilities in Gas Turbine Engines: Operational Experience, Fundamental Mechanisms, and Modeling*, Vol. 210, Progress in Astronautics and Aeronautics, AIAA, Reston, VA, 2005.

[3] Ghoniem, A. F., Annaswamy, A., Wee, D., Yi, T., and Park, S., "Shear Flow-Driven Combustion Instability: Evidence, Simulation, and Modeling," *Proceedings of the Combustion Institute*, Vol. 29, 2002, pp. 53–60.

[4] Lieuwen, T., and Zinn, B. T., "The Role of Equivalence Ratio Oscillation in Driving Combustion Instabilities in Low NO_x Gas Turbines," *Proceedings of the Combustion Institute*, Vol. 27, 1998, pp. 1809–1816.

[5] Huang, Y., Sung, H. G., Hsieh, S. Y., and Yang, V., "Large-Eddy Simulation of Combustion Dynamics of Lean-Premixed Swirl-Stabilized Combustor," *Journal of Propulsion and Power*, Vol. 19, 2003, pp. 782–794.

[6] You, D. N., Huang, Y., and Yang, V., "A Generalized Model of Acoustic Response of Turbulent Premixed Flame and Its Application to Gas-Turbine Combustion Instability Analysis," *Combustion Science and Technology*, Vol. 177, No. 5–6, 2005.

[7] Paschereit, O. C., Gutmark, E., and Weisenstein, W., "Excitation of Thermoacoustic Instabilities by Interaction of Acoustics and Unstable Swirling Flow," *AIAA Journal*, Vol. 38, 2000, pp. 1025–1034.

[8] Stone, C., and Menon, S., "Swirl Control of Combustion Instabilities in a Gas Turbine Combustor," *Proceedings of the Combustion Institute*, Vol. 29, 2002, pp. 155–160.

[9] Stone, C., and Menon, S., "Open Loop Control Combustion Instabilities in a Model Gas Turbine Combustor," *Journal of Turbulence*, Vol. 4, No. 020, 2003.

[10] Pierce, C. D., and Moin, P., "Progress-Variable Approach for Large-Eddy Simulation of Non-Premixed Turbulent Combustion," *Journal of Fluid Mechanics*, Vol. 504, 2004, pp. 73–97.

[11] Selle, L., Lartigue, G., Poinsot, T., Koch, R., Schildmacher, K. U., Kerbs, W., Kaufmann, P., and Veynante, D., "Compressible Large Eddy Simulation of Turbulent Combustion in Complex Geometry on Unstructured Meshes," *Combustion and Flame*, Vol. 137, 2004, pp. 489–505.

[12] Grinstein, F. F., and Fureby, C., "LES Studies of the Flow in a Swirl Combustor," *Proceedings of the Combustion Institute*, Vol. 30, 2005, pp. 1791–1798.

[13] Sommerer, Y., Galley, D., Poinsot, T., Ducruix, S., Lacas, F., and Veynante, D., "Large Eddy Simulation and Experimental Study of Flashback and Blow-Off in a Lean Partially Premixed Swirled Burner," *Journal of Turbulence*, Vol. 5, No. 037, 2004.

[14] Wang, S. W., Hsieh, S. Y., and Yang, V., "Unsteady Flow Evolution in Swirl Injector with Radial Entry, Part 1: Stationary Conditions," *Physics of Fluids*, Vol. 17, No. 4, 2005, 045106.

[15] Wang, S. W., and Yang, V., "Unsteady Flow Evolution in Swirl Injector with Radial Entry, Part 2: External Excitations," *Physics of Fluids*, Vol. 17, No. 4, 2005, 045107.

[16] Huang, Y., and Yang, V., "Bifurcation of Flame Structure in a Lean-Premixed Swirl-Stabilized Combustor: Transition from Stable to Unstable Flame," *Combustion and Flame*, Vol. 136, 2004, pp. 383–389.

[17] Huang, Y., and Yang, V., "Effect of Swirl on Combustion Dynamics in a Lean-Premixed Swirl-Stabilized Combustor," *Proceedings of the Combustion Institute*, Vol. 30, 2005, pp. 1775–1782.

[18] Reynolds, W. C., and Hussain, A. K. M. F., "The Mechanics of an Organized Wave in Turbulent Shear Flow. Part 3. Theoretical Models and Comparisons with Experiments," *Journal of Fluid Mechanics*, Vol. 54, 1972, pp. 263–288.

[19] Liu, J. T. C., "Coherent Structures in Transitional and Turbulent Free Shear Flows," *Annual Review of Fluid Mechanics*, Vol. 21, 1989, pp. 285–315.

[20] Apte, S., and Yang, V., "Unsteady Flow Evolution in Porous Chamber with Surface Mass Injection, Part 2: Acoustic Excitation," *AIAA Journal*, Vol. 40, No. 2, 2002, pp. 244–253.

[21] Chu, B. T., "On the Energy Transfer to Small Disturbances in Fluid Flow (Part I)," *Acta Mechanica*, Vol. 1, 1965, pp. 215–234.

[22] Huang, Y., "Modeling and Simulation of Combustion Dynamics in Lean-Premixed Swirl-Stabilized Gas-Turbine Engines," Ph.D. Dissertation, Dept. of Mechanical Engineering, Pennsylvania State Univ., University Park, PA, 2003.

[23] Erlebacher, G., Hussaini, M. Y., Speziale, C. G., and Zang, T. A., "Toward the Large Eddy Simulation of Compressible Turbulent Flows," *Journal of Fluid Mechanics*, Vol. 238, 1992, pp. 155–158.

[24] Poinsot, T., and Lele, S., "Boundary Conditions for Direct Simulation of Compressible Viscous Flows," *Journal of Computational Physics*, Vol. 101, 1992, pp. 104–129.

[25] Swanson, R. C., and Turkel, E., "On Central Difference and Upwind Schemes," *Journal of Computational Physics*, Vol. 101, 1992, pp. 292–306.

[26] Oefelein, J. C., and Yang, V., "Modeling High-Pressure Mixing and Combustion Processes in Liquid Rocket Engines," *Journal of Propulsion and Power*, Vol. 14, 1998, pp. 843–857.

[27] Apte, S., and Yang, V., "Unsteady Flow Evolution in Porous Chamber with Surface Mass Injection, Part 1: Free Oscillation," *AIAA Journal*, Vol. 39, No. 8, 2001, pp. 1577–1586.

[28]Lu, X., Wang, S., Sung, H., Hsieh, S. Y., and Yang, V., "Large Eddy Simulation of Turbulent Swirling Flows Injected into a Dump Chamber," *Journal of Fluid Mechanics*, Vol. 527, 2005, pp. 171–195.

[29]Apte, S., and Yang, V., "Unsteady Flow Evolution and Combustion Dynamics of Homogeneous Solid Propellant in a Rocket Motor," *Combustion and Flame*, Vol. 131, 2002, pp. 110–131.

[30]Broda, J. C., Seo, S., Santoro, R. J., Shirhattikar, G., and Yang, V., "An Experimental Study of Combustion Dynamics of a Premixed Swirl Injector," *Proceedings of the Combustion Institute*, Vol. 27, 1998, pp. 1849–1856.

[31]Seo, S., "Parametric Study of Lean-Premixed Combustion Instability in a Pressurized Model Gas Turbine Combustor," Ph.D. Dissertation, Dept. of Mechanical Engineering, Pennsylvania State Univ., University Park, PA, 1999.

[32]Chong, M. S., Perry, A. E., and Cantwell, B. J., "A General Classification of Three-Dimensional Flow Field," *Physics of Fluids*, Vol. 2, 1990, pp. 765–777.

[33]Hunt, J. C. R., Wray, A. A., and Moin, P., "Eddies, Stream, and Convergence Zones in Turbulent Flows," Center for Turbulence Research Rept. CTR-S88, 1988, p. 193.

[34]Jeong, J., and Hussain, F., "On the Identification of a Vortex," *Journal of Fluid Mechanics*, Vol. 285, 1995, pp. 69–94.

[35]Liu, T., Huang, Y., and Yang, V., "Linear Stability Analysis of Annular Swirling Jets," *Physics of Fluids* (submitted for publication).

[36]Culick, F. E. C., and Yang, V., "Overview of Combustion Instabilities in Liquid-Propellant Rocket Engines," *Liquid Rocket Engine Combustion Instability*, edited by V. Yang and W. E. Anderson, Vol. 169, Progress in Astronautics and Aeronautics, AIAA, Reston, VA, 1995, Chap. 1, pp. 3–37.

[37]You, D. N., Sun, X. F., and Yang, V., "A Generalized Linear Theory of Three-Dimensional Combustion Instability," *Journal of Fluid Mechanics* (submitted for publication).

[38]Peng, D., Merriman, B., Osher, S., Zhao, H., and Kang, M., "A PDE-Based Fast Local Level-Set Method," *Journal of Computational Physics*, Vol. 155, 1999, pp. 410–438.

[39]Fedkiw, R. P., Sapiro, G., and Shu, C. W., "Shock Capturing, Level Sets, and PDE-Based Methods in Computer Vision and Image Processing: A Review of Osher's Contributions," *Journal of Computational Physics*, Vol. 185, 2003, pp. 309–341.

[40]Sirvoich, L., Kirby, M., and Winter, M., "An Eigen-Function Approach to Large Scale Transitional Structures in Jet Flow," *Physics of Fluids*, Vol. 2, No. 2, 1992, pp. 127–136.

[41]Delville, J., Ukeiley, L., Cordier, L., Bonnet, J. P., and Glauser, M., "Examination of Large-Scale Structures in a Turbulent Plane Mixing Player. Part 1. Proper Orthogonal Decomposition," *Journal of Fluid Mechanics*, Vol. 391, 1999, pp. 91–122.

[42]Citriniti, J. H., and George, W. K., "Reconstruction of the Global Velocity Field in the Axisymmetric Mixing Layer Utilizing the Proper Orthogonal Decomposition," *Journal of Fluid Mechanics*, Vol. 418, 2000, pp. 137–166.

[43]Bonnet, J. P., and Delville, J., "Review of Coherent Structures in Turbulent Free Shear Flows and their Possible Influence on Computational Methods," *Flow, Turbulence and Combustion*, Vol. 66, 2001, pp. 333–353.

[44]Caraballo, E., Samimy, M., Scott, J., Narayanan, S., and DeBonis, J., "Application of Proper Orthogonal Decomposition to a Supersonic Axisymmetric Jet," *AIAA Journal*, Vol. 41, No. 5, 2003, pp. 866–877.

[45]Sirovich, L., "Turbulence and the Dynamics of Coherent Structures, Part 1: Coherent Structures," *Quarterly of Applied Mathematics*, Vol. 45, No. 3, 1987, pp. 561–571.

[46]Frouzakis, C. E., Kevrekidis, Y. G., Lee, J., Boulouchos, K., and Alonso, A. A., "Proper Orthogonal Decomposition of Direct Numerical Simulation Data: Data Reduction and Observer Construction," *Proceedings of the Combustion Institute*, Vol. 28, 2000, pp. 75–81.

[47]Kodal, A., Watson, K. A., Roberts, W. L., and Lyons, K. M., "Turbulence Filter and POD Analysis for Velocity Fields in Lifted CH_4–Air Diffusion Flames," *Flow, Turbulence and Combustion*, Vol. 70 Nos. 1–4, 2003, pp. 21–41.

[48]Berkooz, G., Holmes, P., and Lumley, J. L., "The Proper Orthogonal Decomposition in the Analysis of Turbulent Flows," *Annual Review of Fluid Mechanics*, Vol. 25, 1993, pp. 539–575.

[49]Cordier, L., and Bergmann, M., "Proper Orthogonal Decomposition: an Overview," *Post-Processing of Experimental and Numerical Data*, Lecture Series 2003-03, von Kármán Inst. for Fluid Dynamics, Rhode Saint Genese, Belgium, 2003.

[50]Rowley, C. W., Colonius, T., and Murray, R. M., "Model Reduction for Compressible Flows Using POD and Galerkin Projection," *Physica D*, Vol. 189, 2004, pp. 115–129.

[51]Freund, J. B., and Colonius, T., "POD Analysis of Sound Generation by a Turbulent Jet," AIAA Paper 2002-0072, 2002.

[52]George, W. K., "Insight into the Dynamics of Coherent Structures from a Proper Orthogonal Decomposition," Symposium on Near Wall Turbulence, Dubrovnik, Yugoslavia, May 1988.

[53]Holmes, P., Lumley, J. L., and Berkooz, G., *Turbulence, Coherent Structures, Dynamical Systems and Symmetry*, Cambridge Univ. Press, Cambridge, England, U.K., 1996.

[54]Aubry, N., Guyonnet, R., and Lima, R., "Spatio-Temporal Symmetries and Bifurcation via Bi-Orthogonal Decompositions," *Journal of Nonlinear Science*, Vol. 2, 1992, pp. 183–215.

[55]Rempfer, D., and Fasel, H. F., "Evolution of Three-Dimensional Coherent Structures in a Flat-Plate Boundary Layer," *Journal of Fluid Mechanics*, Vol. 260, 1994, pp. 351–375.

[56]Graham, W. R., Peraire, J., and Tang, K. Y., "Optimal Control of Vortex Shedding Using Low-Order Models, Part 1: Open-Loop Model Development," *International Journal for Numerical Methods in Engineering*, Vol. 44, 1999, pp. 945–972.

N.-S. Liu
Guest Editor